

JGR Solid Earth








RESEARCH ARTICLE

10.1029/2020JB020117

Special Section:

Creep on Continental Faults and Subduction Zones: Geophysics, Geology, and Mechanics

Mechanical Implications of Creep and Partial Coupling on the World's Fastest Slipping Low-Angle Normal Fault in Southeastern Papua New Guinea

James Biemiller¹ , Carolyn Boulton² , Laura Wallace^{1,3} , Susan Ellis³ , Timothy Little², Marcel Mizera^{2,4} , Andre Niemeijer⁴ , and Luc Lavier¹ ¹Institute for Geophysics, Jackson School of Geosciences, University of Texas at Austin, Austin, TX, USA, ²School of Geography, Environment and Earth Sciences, Victoria University of Wellington, Wellington, New Zealand, ³GNS Science, Lower Hutt, New Zealand, ⁴Faculty of Geosciences, Utrecht University, Utrecht, The Netherlands

Key Points:

- GPS velocities reveal horizontal extension of 8.3 ± 1.2 mm/year (~ 8 – 11 mm/year dip-slip) on a low-angle normal fault dipping $\leq 24^\circ$ at the surface
- Shallowest gouges of this fault are frictionally weak and velocity-strengthening; deeper fault rocks are stronger and velocity-weakening
- Fault locking at ~ 5 – 16 km depth with shallower and deeper interseismic creep inferred from geologic, experimental, and geodetic results

Supporting Information:

- Supporting information S1
- Data Set S1
- Data Set S2

Correspondence to:

J. Biemiller,
james.biemiller@utexas.edu

Citation:

Biemiller, J., Boulton, C., Wallace, L., Ellis, S., Little, T., Mizera, M., et al. (2020). Mechanical implications of creep and partial coupling on the world's fastest slipping low-angle normal fault in southeastern Papua New Guinea. *Journal of Geophysical Research: Solid Earth*, 125, e2020JB020117. <https://doi.org/10.1029/2020JB020117>

Received 1 MAY 2020

Accepted 25 SEP 2020

Accepted article online 29 SEP 2020

Abstract We use densely spaced campaign GPS observations and laboratory friction experiments on fault rocks from one of the world's most rapidly slipping low-angle normal faults, the Mai'iu fault in Papua New Guinea, to investigate the nature of interseismic deformation on active low-angle normal faults. GPS velocities reveal 8.3 ± 1.2 mm/year of horizontal extension across the Mai'iu fault, and are fit well by dislocation models with shallow fault locking (above 2 km depth), or by deeper locking (from ~ 5 – 16 km depth) together with shallower creep. Laboratory friction experiments show that gouges from the shallowest portion of the fault zone are predominantly weak and velocity-strengthening, while fault rocks deformed at greater depths are stronger and velocity-weakening. Evaluating the geodetic and friction results together with geophysical and microstructural evidence for mixed-mode seismic and aseismic slip at depth, we find that the Mai'iu fault is most likely strongly locked at depths of ~ 5 – 16 km and creeping updip and downdip of this region. Our results suggest that the Mai'iu fault and other active low-angle normal faults can slip in large ($M_w > 7$) earthquakes despite near-surface interseismic creep on frictionally stable clay-rich gouges.

Plain Language Summary In regions of extension, where tectonic plates pull apart, the Earth's crust breaks along fractures, or "normal faults", that allow parts of the crust to slip past each other. Many of these faults intersect the Earth's surface at a steep angle, but some anomalously low-angle normal faults are oriented at a shallower angle to the surface. Faults can slip during infrequent fast earthquakes or through slower gradual fault creep. Because active low-angle normal faults are rare and typically have low long-term slip-rates, it is not clear whether they cause large earthquakes or creep gradually. Using two approaches, this study addresses whether earthquakes occur on one of the fastest-slipping of these types of faults, the Mai'iu fault in Papua New Guinea. One approach uses GPS measurements to track patterns of displacement of the Earth's surface near the Mai'iu fault over 3 years. Surface displacements confirm that the Mai'iu fault slips actively and are used to constrain models of fault slip at depth. The second approach uses laboratory experiments on rocks from the Mai'iu fault zone to test whether these rocks tend to slip unstably in earthquakes, or creep stably under conditions similar to those in the fault zone. Laboratory results show that rocks from the shallowest parts of the fault tend to creep stably, while deeper fault rocks tend to slip unstably. Combining laboratory, geological, and GPS results to map slip behaviors to different fault zone depths, we find that the Mai'iu fault most likely creeps near the Earth's surface but can generate larger earthquakes at greater depths.

1. Introduction and Background

1.1. Introduction

Active continental rift systems accommodate extension at rates ranging from <1 mm/year to a few cm/year (Abers, 2001; Ruppel, 1995). This extension is facilitated by a variety of seismic and aseismic deformation processes on normal faults, including slip in devastating $M_w 6 +$ earthquakes such as the 6 April 2009 L'Aquila event in Italy that killed over 300 people (Anzidei et al., 2009). Some extending regions, such as the Gulf of Corinth and the Apennines, experience frequent earthquakes on steeply dipping ($>40^\circ$) near-surface fault sections (Abers, 2009; Jackson, 1987; Jackson & McKenzie, 1983). In these same

systems, there is also evidence for aseismic creep on other, less steeply dipping normal faults (Abers, 2009; Hreinsdóttir & Bennett, 2009; Valoroso et al., 2017). Extensional systems commonly consist of a series of near-surface high-angle (dipping 40–70°) normal faults that are at least in part seismogenic, and that sole into a deeper low-angle (<30°) to subhorizontal detachment fault, which may creep aseismically (Abers, 2009; Collettini, 2011; Wernicke, 1995).

The mechanics of initiation and subsequent slip of detachment faults dipping at low angles (<30°) near the Earth's surface are not fully understood. These “low-angle normal faults” (LANFs) appear to defy Mohr-Coulomb friction theory. This theory posits that under a vertical maximum principal stress, normal faults formed in the brittle crust with Byerlee values of friction should initiate at dips of 60–70° and should frictionally lock up and stop slipping at dips <30° (e.g., Axen, 1992, 2004; Wernicke, 1995). However, geologic offsets of ~10 km or more on shallowly dipping detachments are commonly observed globally (e.g., Collettini, 2011; Platt et al., 2015; Wernicke, 1995), and a variety of seismological, geodetic, and geologic observations indicate that some LANFs are active today (e.g., Abers, 2001, 2009; Anderlini et al., 2016; Chiaraluce et al., 2007, 2014; Collettini, 2011; Hreinsdóttir & Bennett, 2009; Numelin, Kirby, et al., 2007; Valoroso et al., 2017; Wallace et al., 2014; Webber et al., 2018). Dip-slip rates of active and inactive LANFs range from <1 to tens of mm/year (Webber et al., 2018). The mechanical paradox of slip on LANFs is most apparent at or near the Earth's surface, where the maximum principal stress is likely to be near-vertical and deformation is assumed to occur predominantly by brittle, frictional failure (e.g., Abers, 2009).

A longstanding and societally important question is whether LANFs can generate large earthquakes and, if so, how frequently (e.g., Wernicke, 1995). The instrumental record of $M_w > 5.5$ normal-fault earthquakes with unambiguously discriminated rupture planes is sparse (Collettini et al., 2019; Jackson & White, 1989), but it includes two events in the Gulf of Corinth with reported dips as low as 30° and 33°, and with magnitudes of 5.9 and 6.2, respectively. Other earthquakes with indiscriminate nodal planes are inferred to reflect LANF slip based on their seismological and geological context (Collettini, 2011), including the notable 29 October 1985 M_w 6.8 Woodlark Basin earthquake. This event occurred around a seismologically imaged LANF, aligned parallel to one of the focal planes, and may be the largest LANF earthquake documented globally (Abers, 2001; Abers et al., 1997).

Due to the rarity and typically low slip rates (a few mm/year or less) of active LANFs (Webber et al., 2018), geodetic observations across them are scarce and can be difficult to interpret. However, available results indicate some degree of aseismic creep on the active Altotiberina LANF in the Northern Apennines, Italy (Anderlini et al., 2016; Chiaraluce et al., 2014; Hreinsdóttir & Bennett, 2009; Valoroso et al., 2017). GPS velocities have been used to infer that this fault actively slips at 1.5 (Anderlini et al., 2016) to 2.4 mm/year (Hreinsdóttir & Bennett, 2009). Hreinsdóttir and Bennett (2009) used dislocation modeling of GPS velocities to infer that slip on the Altotiberina fault occurs predominantly by aseismic creep below a locking depth of 4 km; however, Anderlini et al. (2016) showed that these velocities are better fit by models with heterogeneous coupling and partial creep on the Altotiberina fault and splay faults in its hanging wall.

A variety of mechanisms have been proposed for aseismic creep on LANFs. These include the following: (1) an enhanced tendency for stable slip resulting from elevated pore-fluid pressures (Abers, 2009; Axen, 1992; Collettini & Barchi, 2004; Ikari et al., 2009); (2) rotated principal stress orientations favoring slip on low-angle faults (Axen, 1992, 2020); and/or (3) creep on interconnected networks of frictionally stable minerals (e.g., Collettini, 2011; Collettini et al., 2019) such as talc (Collettini, Niemeijer, et al., 2009), clays (Ikari et al., 2009; Ikari & Kopf, 2017), or serpentine (antigorite/lizardite) (Floyd et al., 2001). It remains unclear whether fault rocks composed of these frictionally stable mineralogies are abundant on active LANFs; and, in particular, whether they are present (or thermodynamically stable) at the depths where LANFs are inferred to be creeping. One promising approach to understanding mechanisms of LANF slip involves the integration of friction experiments and microstructural analyses of rocks exhumed along an active LANF with corresponding geodetic observations of surface deformation around the same fault. Such an integrated approach has the potential to illuminate the mechanics and spatial extent of active LANF slip. Evaluating these disparate data sets in tandem can help connect geodetic signals of LANF slip to geologically and experimentally constrained deformation mechanisms.

Here we address the question of whether LANFs creep aseismically or slip in earthquakes following periods of locking and interseismic elastic strain accumulation by presenting and modeling data from a dense

campaign GPS network spanning the world's most rapidly slipping active LANF, the Mai'iu fault in south-east Papua New Guinea (PNG; Webber et al., 2018). To strengthen our interpretation of the geodetic data, we perform hydrothermal velocity-stepping friction experiments on exhumed samples from different parts of the Mai'iu fault rock sequence under a range of relevant crustal conditions. Our results complement new microstructural observations of deformation mechanisms within the Mai'iu fault rocks in Mizera, Little, Boulton, Prior, et al. (2020). Geological and geodetic evidence suggests that the Mai'iu fault slips at dip-slip rates of ~ 10 mm/year (Wallace et al., 2014; Webber et al., 2018). The Mai'iu fault is therefore an ideal natural laboratory in which to use both geology and geodesy to study the nature of interseismic deformation on an active crustal-scale, misoriented fault. We employ detailed geodetic surveys, elastic dislocation modeling techniques, and laboratory friction experiments on rocks from the Mai'iu fault to address the mechanics and seismic behavior of a rapidly slipping, active LANF.

1.2. Tectonic and Geological Setting of the Mai'iu Fault

The Woodlark Rift in southeast PNG is a young, actively propagating rift located within a region of microplates between the converging Pacific and Australian plates (Figure 1a; Baldwin et al., 2012, and references within) and is well known for hosting active LANFs near its westward transition from oceanic spreading to continental rifting (Abers, 1991, 2001; Abers et al., 1997, 2016; Little et al., 2007). Northward subduction of Solomon Sea oceanic lithosphere at the San Cristobal and New Britain trenches drives rapid counterclockwise rotation of the Woodlark and Trobriand microplates at $2\text{--}2.7^\circ/\text{Myr}$ relative to Australia about nearby Euler poles to the SW (Figure 1a), yielding primarily N-S extension in the Woodlark Rift. Extension rates range from 20–35 mm/year in the eastern Woodlark spreading center to 5–15 mm/year in the onshore continental portion of the rift in the Papuan Peninsula and D'Entrecasteaux Islands (Wallace et al., 2014). Recent seismicity is focused just west of the oceanic-continental rift transition, following the Woodlark Rise westward through the D'Entrecasteaux Islands (Figure 1d; Abers et al., 1997, 2016). This seismicity commonly aligns with geologically mapped and/or geodetically inferred active normal faults or strike-slip transfer faults (Little et al., 2007, 2011; Wallace et al., 2014). From Goodenough Island west to Cape Vogel, microseismicity focused in the upper 15 km along a WSW-trending corridor termed the Ward Hunt Strait fault zone delineates a possible actively deforming transfer zone in continental crust near the Papuan Peninsula (Abers et al., 2016; Figures 1b and 1d). Few shallow (<12 km) earthquakes have been observed to the west of the Ward Hunt Strait fault zone, where most extension appears to collapse onto a single fault—the low-angle Mai'iu fault. Offshore to the northeast of the Mai'iu fault trace, aligned microseismicity from 12–25 km depth outlines a $30\text{--}40^\circ$ -dipping planar zone inferred to be the downdip extent of the Mai'iu fault (Figure 1d; Abers et al., 2016).

Dipping $\sim 21^\circ$ where it intersects the Earth's surface, the Mai'iu fault is the dominant mapped fault in the continental Woodlark rift between 149.0 and 149.6°E (Figure 1; Abers et al., 2016; Little et al., 2019; Mizera et al., 2019; Wallace et al., 2014). The footwall of the Mai'iu fault hosts the actively exhuming Dayman-Suckling metamorphic core complex, a smoothly corrugated domal structure exposing very low-grade (pumpellyite-actinolite-facies) rocks near its ~ 3 -km-high crest and higher-temperature (greenschist-facies) rocks along its northern margin near sea level (Daczko et al., 2009; Little et al., 2019). The Mai'iu fault juxtaposes metabasaltic rocks—the Goropu Metabasalt—in its footwall against ultramafic rocks of the Papuan Ultramafic Belt, and structurally above, unmetamorphosed conglomeratic rocks in its hanging wall (e.g., Little et al., 2019; Mizera, Little, Boulton, Prior, et al., 2020). Over the past few Myr, the Mai'iu fault is inferred to have slipped at ~ 12 mm/year, based on the slip-parallel width (at least 30 km) of exhumed fault remnants atop the Dayman-Suckling metamorphic core complex and the exposure at >2 km elevation of 2–3 Ma syn-extensional granites in the footwall that were originally buried at depths of 4–10 km (Little et al., 2019; Mizera et al., 2019; Osterle et al., 2020). In addition, accumulation of cosmogenic nuclides in quartz veins on the exhumed fault scarp of the Mai'iu fault indicate Holocene to present-day dip-slip rates of 11.7 ± 3.5 mm/year (Webber et al., 2018). For a 21° dip, modern dip-slip rates of 7.5–9.6 mm/year across the Mai'iu fault have been estimated from a regional-scale network of GPS velocities (Wallace et al., 2014) and agree well with geologic slip rates.

Minor synthetic and antithetic splay faults in the hanging wall of the Mai'iu fault are presumed to intersect the active fault at depths of up to a few km (Figure 1; Little et al., 2019; Mizera et al., 2019). The most prominent of these, the Gwoira fault, cuts the upper ~ 1 km of the Mai'iu fault hanging wall east of Mt.

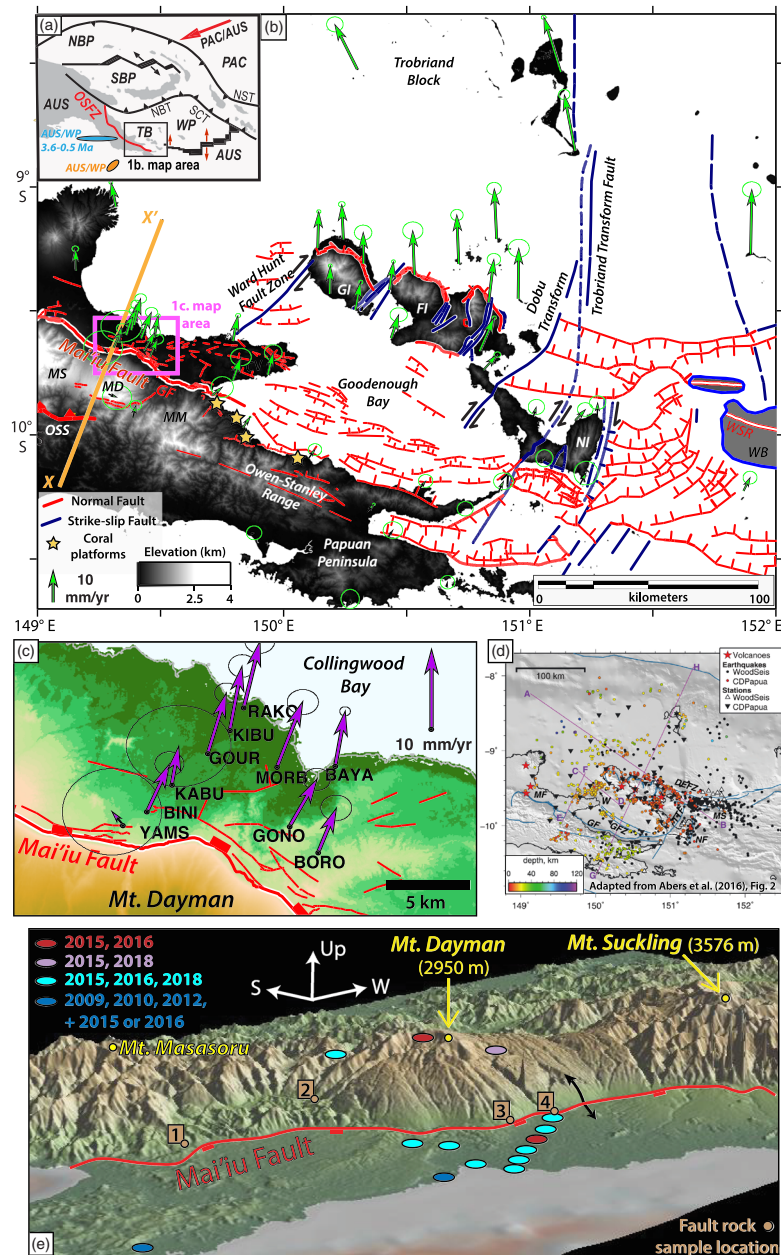


Figure 1. (a) Regional tectonic map of PNG with main map area outlined, showing overall Australia-Pacific Plate convergence and Woodlark spreading (vectors). Ellipses show modern (orange; Wallace et al., 2014) and 3.6–0.5 Ma (cyan; B. Taylor et al., 1999) poles of rotation of the Woodlark Plate relative to the Australian Plate. (b) Topographic map with faults from Little et al. (2007, 2011, 2019) and GPS velocities relative to the Australian Plate (section 2; Wallace et al., 2014). Ellipses show 95% confidence intervals based on formal uncertainties. Stars indicate uplifted Holocene coral platforms. Dashed box shows area of (c). (c) Enlarged map of dense GPS velocity field on the Mai'iu fault hanging wall. (d) Regional map showing seismicity and seismometer locations from Abers et al. (2016). (e) Oblique view of the Mai'iu fault and Dayman-Suckling Metamorphic Core Complex (Mt. Masasoru, Mt. Dayman, and Mt. Suckling). Black arrows show sense of motion across the fault. Ellipse colors show observation years at GPS sites near the fault (see key), and brown circles show fault rock sample locations. Samples from each site include the following: (1) PNG-15-70; (2) PNG-14-19E, PNG-14-19F, and PNG-16-17D2H; (3) PNG-14-33A and PNG-14-33B; (4) PNG-15-50B and PNG-16-151e from adjacent sites; see supporting information Figure S6 for details. Topography from 90-m SRTM (Shuttle Radar Topography Mission) data and GeoMapApp (<http://www.geomapapp.org>). AUS = Australian Plate; PAC = Pacific Plate; NBP = North Bismarck Plate; SBP = South Bismarck Plate; WP = Woodlark Plate; NBT = New Britain Trench; SCT = San Cristobal Trench; MF = Mai'iu fault; GF = Gwoira fault; MS = Mt. Suckling; MD = Mt. Dayman; MM = Mt. Masasoru; OSS = Owen-Stanley Suture zone; GI = Goodenough Island; FI = Fergusson Island; NI = Normanby Island; TB = Trobriand Block; WSR = Woodlark Spreading Ridge; WB = Woodlark Basin.

Dayman (Webber et al., 2020). Inception of this splay fault led to abandonment of the shallowest portion of the Mai'iu fault farther south. East of the Gwoira fault, the Mai'iu fault system steps offshore and remains active along the southern Goodenough Bay coastline, as evidenced by Holocene uplift of coral reef terraces at rates of up to 4.3 mm/year (Biemiller et al., 2018; Mann et al., 2009; Mann & Taylor, 2002). The well-preserved platform-notch-platform morphology and clustered $^{230}\text{Th}/^{234}\text{U}$ ages of these emerged reefs reflect episodic and presumably coseismic meter-scale uplift events, suggesting that the Goodenough Bay segment of the Mai'iu fault system slips in moderately large ($M_w > 7$) earthquakes (Biemiller et al., 2018).

1.3. Mai'iu Fault Rock Sequence and Deformation Mechanisms

Little et al. (2019) details the exhumed Mai'iu fault rock sequence. Working structurally upward and toward the most recently formed part of the sequence, this includes a mafic mylonite zone (1 to several tens of meters thick), a layer of foliated cataclasite-breccia (<2 m thick), an ultracataclasite layer (~40 cm thick), and mineralogically variable fault gouges immediately below the principal displacement surface of the fault (<20 cm thick; see section 3.1 for more details of this sequence). The arrangement of progressively lower-temperature fault rocks narrowing upward (normal to the fault surface) is interpreted as a time sequence of strain localization, where the higher units are more shallowly derived and have cannibalized those underlying them (Little et al., 2019).

The mylonitic rocks are LS-tectonites that have a strong NNE-trending stretching lineation and normal-sense shear fabrics (Little et al., 2019). Pseudosection modeling of the greenschist-facies mineral assemblage (epidote, actinolite, chlorite, albite, titanite, \pm quartz, \pm calcite) in the mafic mylonites indicates peak metamorphic conditions of $\sim 425 \pm 50^\circ\text{C}$ and 5.9–7.2 kbar. The mafic mylonites rocks are inferred to have been exhumed from $\sim 25 \pm 5$ km depth, yielding a depth-averaged geothermal gradient of $\sim 17^\circ\text{C}/\text{km}$ (Daczko et al., 2009). Microstructural analyses indicate that Neogene and younger shearing in the polyphase mafic mineral assemblage comprising the mylonite zone was accomplished by diffusion-accommodated grain-boundary sliding (along epidote, actinolite, chlorite, and albite grains; see Mizera, Little, Boulton, Prior, et al., 2020) together with syntectonic chlorite precipitation at temperatures $> 270^\circ\text{C}$ (Little et al., 2019; Mizera, Little, Boulton, Prior, et al., 2020). The mylonite zone was overprinted and brittlely reworked into the structurally overlying foliated cataclasites.

The foliated cataclasites host abundant pseudotachylite veins that indicate prior seismic slip on the Mai'iu fault. $^{40}\text{Ar}/^{39}\text{Ar}$ ages for two pseudotachylite veins are ~ 2.2 Ma (Little et al., 2019). Given the dip-slip rate of ~ 10 mm/year, these ages suggest pseudotachylite formation (i.e., seismic slip) at depths of ~ 10 – 12 km (Little et al., 2019; Webber et al., 2018). Geothermometry measurements obtained from syntectonic chlorite in the foliated cataclasites reveal an average temperature of $273 \pm 46^\circ\text{C}$ (1σ), yielding a mean geothermal gradient of $\sim 22 \pm 4^\circ\text{C}/\text{km}$ if they were active at 10 – 12 km depth, where the mutually cross-cutting pseudotachylite veins formed (Mizera, Little, Boulton, Prior, et al., 2020).

Cross-cutting relationships between pseudotachylite veins, ultramylonite bands, and ductilely sheared calcite extension veins in the foliated cataclasite layer imply mixed-mode seismic and aseismic slip, and have been used to infer a peak in fault strength near the brittle-ductile transition (Little et al., 2019; Mizera, Little, Boulton, Prior, et al., 2020). Such a strength peak at ~ 10 – 12 km depth approximately coincides with the updip end of the corridor of microseismicity that Abers et al. (2016) attribute to the Mai'iu fault at depths of 12 – 25 km (Figure 1d). Gouges comprise the principal slip zone in outcrops. The gouges are not cut by veins or folded by any of the foliations present in the underlying units, suggesting that these gouges formed and slipped during latest stages of deformation in the uppermost few km of the fault zone. Overall, microstructural analyses of the Mai'iu fault rock sequence reveal that the fault zone accommodates shear strain in both seismic slip and aseismic creep via a complex synexhumational series of frictional-viscous deformation mechanisms.

2. Campaign GPS Experiment

2.1. GPS Data and Velocities

In 2015, a network of 12 new campaign GPS monuments was installed near Mt. Dayman, ranging from the domal footwall of the Mai'iu fault northward across the fault trace into the lowlands of the hanging wall and the coast of Collingwood Bay (Figure 1e). The network was designed with densest station spacing in the

lowlands to resolve any signal of elastic strain accumulation in the hanging wall of the Mai'iu fault. Stations were installed with station spacings of 3–5 km subparallel to fault slip direction (NNE, Figure 1e). We measured all these sites in 2015 and remeasured most of them in 2016 and 2018 using Zephyr geodetic antennas with Trimble 5700 and R7 receivers. Due to the absence of road access in the area, all of the lowland sites were visited on foot and the high mountain footwall sites were accessed via helicopter and on foot. All observations lasted at least 2 days, with most lasting three or more. A few of the sites were destroyed over the course of the study: URJA was destroyed between 2015 and 2016 (after the first measurement; no velocities were derived from this site and it is not included in any velocity plots), and KABU and DD01 were destroyed between 2016 and 2018 (after the second measurement). Additionally, we remeasured seven previously established sites (Wallace et al., 2014), extending the time series of these original sites and helping tie the new sites into the preexisting regional campaign GPS network. We incorporated campaign GPS data collected at 40 sites between 2009 and 2012 by Wallace et al. (2014), as well as data from a few sites measured by Australian National University prior to 2009. The sites and years of all campaign data are listed in Table S1.

Data were processed and aligned with the global reference frame ITRF14 using the GAMIT and GLOBK software packages (Herring et al., 2015, 2018). We used GAMIT to estimate orbital and rotational parameters, neutral atmospheric delays, and phase ambiguities to solve for the relative positions and covariance matrices of sites in our network. We also accounted for ocean tidal loading (from Onsala Space Observatory, <http://holt.oso.chalmers.se/loading/>) in the processing. These relative solutions were combined with solutions generated by the MIT processing center (Herring et al., 2016) from IGS global continuous GPS stations using a global Kalman filter, GLOBK, placing tight constraints on the positions of a subset of well-established global IGS network sites in order to tie our site positions into the ITRF14 reference frame. Site velocities were estimated from time series of daily position solutions. Formal uncertainties were augmented to account for random-walk noise (e.g., following approaches used by Beavan et al., 2016; Koulali et al., 2015; Williams et al., 2004; Zhang et al., 1997; see Text S1).

To correct for static coseismic displacements at our sites due to regional large earthquakes (e.g., Banerjee et al., 2005; Tregoning et al., 2013), we used STATIC1D (Pollitz, 1996) to calculate the surface displacement at each site due to static elastic interactions from planar dislocations in a spherical layered half-space with PREM elastic stratification (Dziewonski & Anderson, 1981), representing fault slip in the 2007 M_w 8.1 Solomon Islands earthquake and all M_w 6.9 + earthquakes from 2009 to July 2018 (Hayes, 2017; Lay et al., 2017; Lee et al., 2018; Strasser et al., 2010; F. W. Taylor et al., 2008; U.S. Geological Survey, 2019; Wallace et al., 2015). These regional earthquakes were between 350 and 825 km away from our local network spanning the Mai'iu fault. See Text S2 for details.

Relative to a fixed Australian Plate, horizontal velocities for sites on the hanging wall of the Mai'iu fault trend NNE, approximately perpendicular to the fault trace. These velocities generally align with previously reported velocities showing southeast PNG rotating counterclockwise relative to the Australian Plate around a nearby Euler pole (Figures 1 and 2; Wallace et al., 2014). Hanging wall velocities gradually increase with strike-perpendicular distance northward from the fault trace and show 8.3 ± 1.2 mm/year of NNE-SSW horizontal extension across the fault, measured from the elastic block models (section 2.2) as the horizontal extension rate perpendicular to the strike of the modeled Mai'iu fault in Figure 2a. This extension rate corresponds to 7.6–10.2 mm/year dip-slip rates for a 21°-dipping fault. One outlier is the hanging wall site nearest to the fault trace, YAMS, which shows subtle NNW motion, but this velocity is based on only 2 years of observation and therefore has higher uncertainty than most other sites in the network.

2.2. Elastic Block and Dislocation Modeling Approaches

We undertake two different approaches to modeling the GPS velocity data to investigate the degree of interseismic coupling and slip rates on the Mai'iu fault. To tie our velocities into a regionally kinematically consistent reference frame, we first use an elastic block modeling approach (similar to Wallace et al., 2014). After establishing a fixed-footwall reference frame using the elastic block model, we use simpler 2-D elastic dislocation models to determine the Mai'iu fault properties that best explained the observed surface velocity data (similar to Hreinsdóttir & Bennett, 2009).

In the elastic block models, we represent the tectonic deformation responsible for GPS velocities in southeast PNG as the interactions between adjacent elastic crustal blocks, with each rotating about an independent

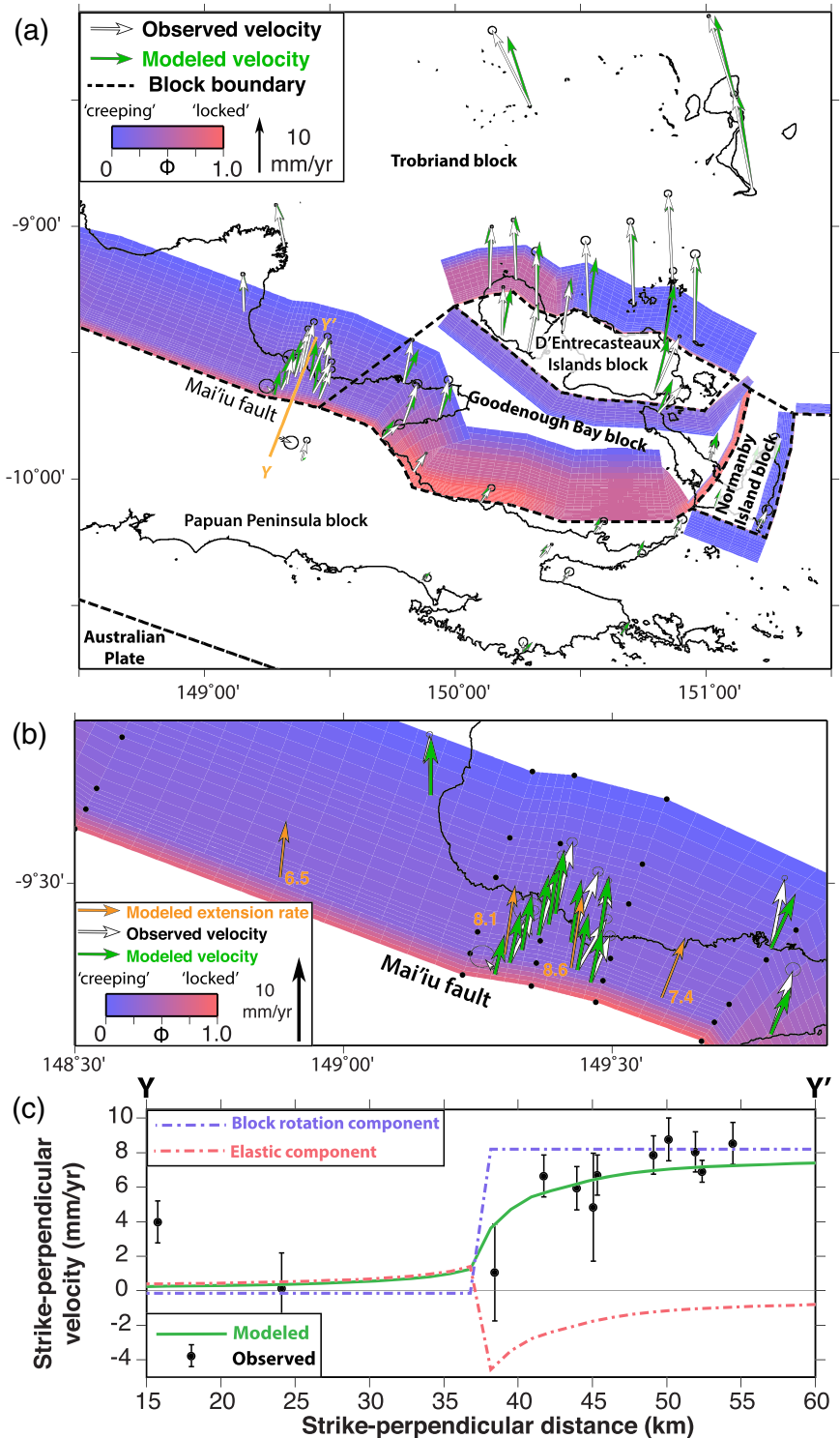


Figure 2. Best-fitting elastic block fault locking model results colored by kinematic fault coupling ratio Φ . Vectors indicate observed (white) and predicted (green) GPS velocities. (a) Preferred locking model. Dashed lines show preferred block boundaries (Figure S3; Table S3). (b) Enlarged view of GPS velocities near the modeled Mai'iu fault, which is predominantly uncoupled below 2 km depth. Labeled orange vectors show modeled rates and directions of relative motion between adjacent blocks across the fault. (c) Strike-perpendicular horizontal velocities relative to the Papuan Peninsula footwall block for sites in the Mai'iu fault network (Profile Y-Y' in (a)). Observed velocities (black), modeled velocities (green), and the modeled velocity contribution of elastic strain (pink) and block rotations (purple) are shown.

Euler pole of rotation. Although we are most interested in near-field deformation associated with the Mai'iu fault, our wider data set spans the broader southeast PNG region where crustal deformation can be described by the rotations and interactions between numerous microplates and crustal blocks (Wallace et al., 2014; Figures 1 and 2a). Therefore, we model multiple crustal blocks (Figure 2a) and invert the GPS velocities for poles of rotation for each block relative to the Australian Plate (our velocities are in an Australia-fixed reference frame).

In these crustal block models, elastic strains accumulated along block boundaries are modeled as back slip on block-bounding faults and parameterized by the kinematic fault coupling ratio, Φ , which describes the fraction of predicted relative plate motion that is accrued as a slip deficit rate. For example, if $\Phi = 0$, the fault is creeping at full plate motion rate, while if $\Phi = 1$, there is no creep in the interseismic period of our GPS measurements and the fault is fully locked. The slip deficit rate is simply the coupling ratio multiplied by the long-term slip rate on the fault from the crustal block motions. We use TDEFNODE (McCaffrey, 2009) to jointly invert for the block poles of rotation and the spatial distribution of Φ on block-bounding faults. The model is constrained by kinematic data including GPS velocities, earthquake slip vectors, and transform fault orientations from throughout the southeast PNG region.

Block boundaries and fault geometries are defined on the basis of regional tectonics, field mapping studies, and geophysical constraints such as seismicity. For this model, block and fault geometries are based largely on those of Wallace et al. (2014), although some geometries such as the position and dips of the Mai'iu fault have been updated based on recent field mapping (Little et al., 2019; Mizera et al., 2019; Webber et al., 2018, 2020) and seismological observations (Abers et al., 2016). The statistical significance of various block configurations is tested with an F test for block independence (Figures 2a and S3; Table S5). We utilize our preferred configuration for subsequent models testing fault coupling (Figure 2a).

Joint inversion of diverse local and regional kinematic data sets within a block model framework helps to ensure that modeled block rotations and fault coupling are consistent with both regional tectonic motions and local observations. In addition, simple 2-D planar dislocation fault models can provide focused insight into the tradeoffs between slip rate, locking depth, and fault geometry, especially for dense GPS networks that span major active faults. For this reason, we also perform a simple inversion of strike-perpendicular GPS velocities across the Mai'iu fault for fault dip, locking depth, and dip-slip rate using the solutions for planar dislocations in an elastic half-space from Okada (1985). This simplified 2-D approach has been used to model GPS velocities related to slip on other LANFs (Hreinsdóttir & Bennett, 2009) and reverse and strike-slip faults (Beavan et al., 1999). In such models, a single fault is represented as a 2-D planar dislocation that extends infinitely in the third dimension. In our case, predicted elastic contributions to surface displacement due to interseismic back slip on the locked dislocations are added to the long-term fault-strike-perpendicular plate motion rate and compared with observed surface velocities to calculate the misfit between the model and the data. By minimizing the data misfit as expressed by the reduced χ^2 , these models highlight the range of fault properties and locking most likely responsible for observed surface displacements. The calculated χ^2 is minimized through an extensive grid search of the three fault parameters (dip, slip rate, and locking distribution), as discussed in section 3.2.

2.3. Elastic Block Model Results

Our preferred elastic block model treats Fergusson/Goodenough Islands, Normanby Island, Goodenough Bay, and the Papuan Peninsula as discrete independent crustal blocks, similar to that of Wallace et al. (2014). More complex configurations (with additional blocks) do not produce a statistically significant improvement in fit to the data (see F tests and results in Figures 2a and S3; Table S5). The best-fitting model of jointly inverted block poles of rotation and fault locking are shown in Figure 2a, indicating 8.3 ± 1.2 mm/year of horizontal extension across the Mai'iu fault. This model predicts locking of the western segment of the Mai'iu fault down to only 2 km depth, below which the fault creeps. Deeper locking occurs on the eastern segment through Goodenough Bay and the faults immediately north of Goodenough Island, although this is not well constrained due to a relative lack of GPS sites on the largely submarine hanging wall east of our study area.

Inversions producing the model in Figure 2 allow fault coupling ratios to vary from 0–1, but they impose a constraint that coupling decreases with increasing depth. To test how such assumptions affect the preferred

locking model, additional inversions were performed with different constraints on locking, such as allowing coupling to vary freely with depth or assuming a discrete and uniform locking depth (Text S3; Figure S4). The large misfit of models with prescribed locking depths from the surface to >2 km confirm that campaign GPS velocities are inconsistent with Mai'iu fault locking from the surface to more than a few km depth. Inversions with fewer imposed locking constraints, including those in which no downdip decrease in coupling is prescribed (i.e., no assumption that the fault is locked at the surface), all converge on best-fitting models with shallow locking to <2 km depth (Figure S4), compatible with a LANF creeping at most depths. To test how the higher uncertainty in velocity at site YAMS affects these inversion results, we also performed inversions that excluded YAMS and found that they yield similar results: the Mai'iu fault predominantly creeps below a shallow locking depth (~ 2 km) in the best-fitting model with $\chi^2 = 1.70$ (Figure S4i).

2.4. The 2-D Dislocation Modeling

2.4.1. Model 1: Locked-to-Surface Models

Modeled crustal block rotations help to establish a footwall-fixed reference frame in which explore Mai'iu fault locking in more detail using 2-D dislocation models. We compare the predicted horizontal surface velocities (now in a footwall-fixed reference frame) from 128,000 two-dimensional elastic half-space planar dislocation models to the strike-perpendicular GPS velocities from sites within a 65 km strike-perpendicular distance of the Mai'iu fault trace along profile X-X' (Figure 1b). This approach offers a focused look at how modeled fault properties affect the fit to GPS velocities, but does not account for 3-D factors such as along-strike variations in fault geometry or locking. We first test the slip rate, dip angle, and locking depth of a single fault locked to the Earth's surface, as in previous GPS studies of LANF locking (Hreinsdóttir & Bennett, 2009). Although the shallow ($\leq 24^\circ$) dip of the Mai'iu fault along its trace is well constrained (Little et al., 2019; Mizera et al., 2019), the fault surface exhumed on the Dayman-Suckling metamorphic core complex steepens northward (Webber et al., 2020), and fault-related microseismicity implies a similar northward steepening dip (Figure 1d; Abers et al., 2016). We therefore allow the modeled fault dip to vary in order to more fully explore the parameter space. We test fault dip angles ranging from 1 – 80° in 1° increments, dip-slip rates of 0.5 – 20 mm/year in 0.5 mm/year increments, and locking depths of 0.5 – 20 km in 0.5 km increments (Figures 4a and S6). For the strike-perpendicular horizontal velocities, the best-fitting (minimum $\chi^2 = 0.94$) modeled fault dips 26° is locked down to 2 km depth, and slips at 10 mm/year below this depth (model 1; Figures 3a–3c). This result indicates that the observed GPS horizontal velocities can be explained by active aseismic creep below a shallow locking depth on a gently dipping normal fault. The close match between the best-fit model's fault dip and the geologically inferred fault dip supports this result. Vertical velocities (which have high uncertainties) are modeled (Figures 3b and 3e) but not used to constrain the grid search. Joint modeling of vertical and horizontal components (e.g., Beavan et al., 2010; Bennett et al., 2007; Segall, 2010; Serpelloni et al., 2013) yields similar locking results (Text S4). Note that the best-fit $\chi^2 < 1.0$ suggests that the random-walk noise model may slightly overestimate the velocity uncertainty corrections, particularly for campaign sites with only 2 or 3 years of observations.

2.4.2. Model 2: Consideration of Shallow Creep and Splay Fault Activity

The setup of model 1 is inherently limited by the assumptions that the fault is locked at the surface and that only one planar structure is active, which may not be appropriate for this and other LANF systems. The hanging walls of major detachment faults are commonly cut by minor splay faults that may variably slip or creep (e.g., Anderlini et al., 2016). In the case of the Mai'iu fault, discontinuous splay faults have been mapped in parts of the hanging wall (Figure 1b; Little et al., 2019; Webber et al., 2020). Additionally, the shallow portions of many LANFs, including the Mai'iu fault (sections 3.2–3.3), contain gouges of weak, frictionally stable mineralogies that may promote near-surface aseismic creep (Collettini, 2011, and references within; Little et al., 2019). To test whether these mechanisms allow aseismic creep in the near-surface portions of the Mai'iu fault and/or its splay faults, we develop buried dislocation models that do not require full fault locking at the Earth's surface and that allow for slip on adjacent splay faults (model 2).

Our buried dislocation models allow for creep both updip and downdip of a locked patch or “asperity” (e.g., Collettini et al., 2019). Because the velocity at YAMS is more consistent with footwall motion, we treat it as a footwall site in these models: essentially, this treatment considers the possibility that, in the shallowest subsurface, creep may transfer from the main Mai'iu fault to one of the many active splay faults in the hanging wall, some of which are <1 km from the main fault trace (Little et al., 2019). The modeled fault trace is hence projected between sites YAMS and BINI in order to incorporate YAMS into the footwall. Note that in all

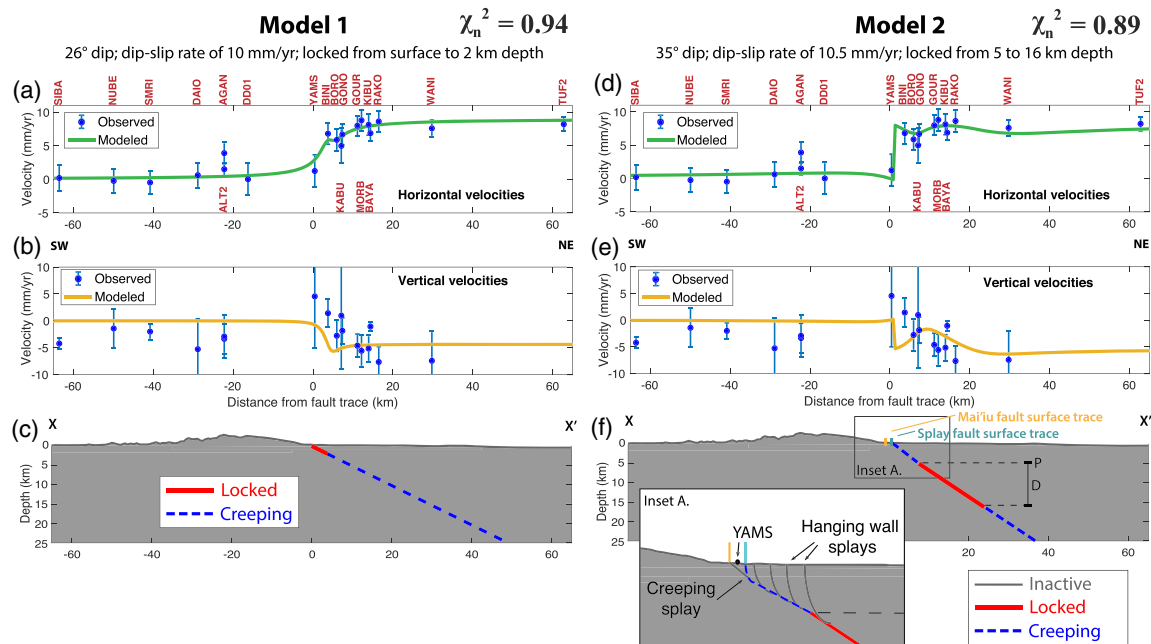


Figure 3. Best-fitting 2-D planar elastic half-space dislocation locking models based on strike-perpendicular horizontal velocities projected onto profile X-X' of Figure 1b. Red labels show GPS site names. (a–c) Model 1; locked to 2 km depth. (d–f) Model 2; locked from 5 to 16 km depth, with creep and splay fault slip above 5 km depth. (a, d) Observed (blue) and modeled strike-perpendicular velocities. (b, e) Observed and modeled vertical velocities. (c, f) Schematic of fault locking models. Profile topography from 90-m SRTM data and GeoMapApp (<http://www.geomapp.org>).

buried dislocation scenarios, the data-fit improves significantly by treating site YAMS as part of the footwall: for models based on the horizontal velocities, χ^2 decreases from 0.95 with YAMS in the hanging wall to 0.89 with YAMS in the footwall. The best-fit buried dislocation model (model 2; $\chi^2 = 0.89$; Figures 3d–3f) fits the horizontal velocities better than the best-fit model with locking imposed at the surface (model 1; $\chi^2 = 0.94$; Figures 3a–3c). The best-fit model with a buried locked zone involves a 35°-dipping fault, locked from 5 to 16 km depth and slipping at 10.5 mm/year updip and downdip of the locked zone (Figures 3d–3f), consistent with microseismic, structural, and surface modeling evidence that the Mai'iu fault steepens to dip 30–40° between ~5 and 12 km depth (Abers et al., 2016; Little et al., 2019; Webber et al., 2020). Fixing fault dip to a geologically and geodetically reasonable average crustal dip of 35°, Figure 4b shows tradeoffs between the total depth range of locking (depth range D, Figure 3f), the depth of the updip limit of locking (depth P, Figure 3f), and slip rate. We note that in future work the uncertainty in shallow fault slip behavior could be reduced by remeasuring the hanging wall site nearest to the fault trace, YAMS, in order to derive a more meaningful secular velocity above the shallowest fault zone; nonetheless, despite its high uncertainty, the velocity of YAMS still helps constrain the range of possible secular velocities near the fault trace and is used in the preferred kinematic model inversions. To determine the effects of this velocity on the kinematic model results, inversions were performed using all velocities except YAMS (Figures S9 and S10). These inversions yield less of a distinction between the two preferred locking scenarios of Models 1 and 2: shallow near-surface locking with deeper creep or stronger locking at depth with creep updip and downdip of the strongly locked region (Figure S10c). Although the specific fault parameters of the best-fitting models vary slightly when YAMS is excluded, the two preferred models are strikingly similar to the best-fitting Models 1 and 2 based on inversions that included YAMS (Figure 3). Geologic, experimental, and seismological evidence help distinguish between these two families of kinematic models (section 4.2).

Model 2 assumes that interseismic fault creep updip of a more strongly locked region is mechanically feasible. Shallow interseismic fault creep occurs above locked seismogenic patches on a variety of faults (Harris, 2017), including the strike-slip Hayward fault in California (Harris, 2017, and references within) and the Nankai subduction megathrust, where periodic slow-slip events near the trench occur updip of the locked portion of the megathrust (Araki et al., 2017). However, recent analytical models predict a strong

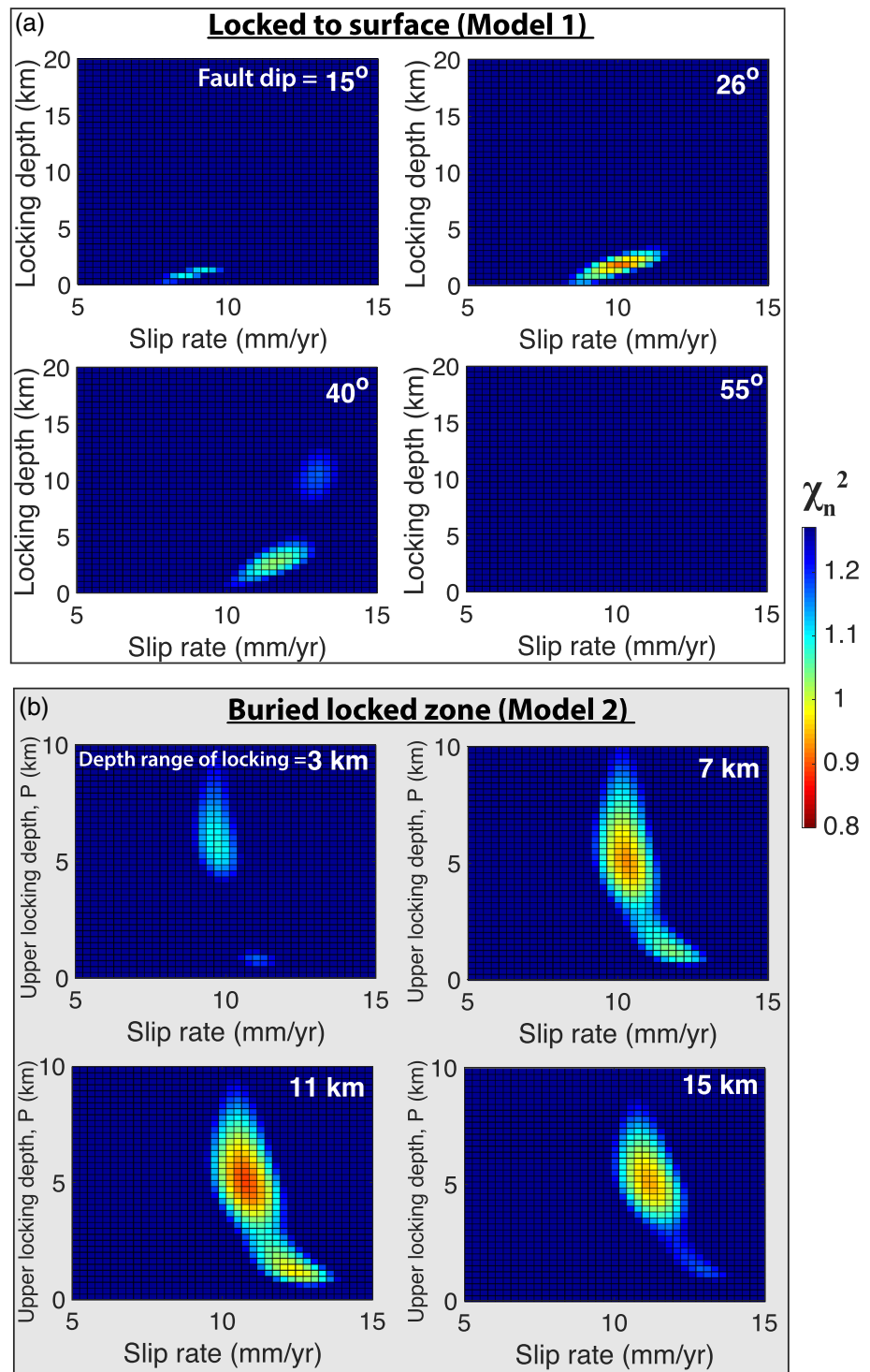


Figure 4. Example of misfit (χ^2) tradeoffs for 2-D dislocation models capped at $\chi^2 = 1.27$ (equivalent to 75% confidence interval for model 2 calculated with F tests for statistical significance) to highlight those models that fit the data reasonably well. (a) Tradeoffs between locking depth and slip rate for locked from surface to depth models with different dip angles. Locked-at-surface models prefer shallow locking (<4 km depth) on a shallowly dipping ($\sim 26^\circ$) fault slipping ~ 9 – 12 mm/year, while steeply dipping faults ($\geq 40^\circ$) do not fit the data well ($\chi^2 > 1.0$). (b) Buried-dislocation models show tradeoffs between the updip depth of locking (depth P , Figure 3f) and slip rate with different depth ranges of locking (depth D , Figure 3f). Fault dip shown here is fixed to the best-fitting value of 35° ; however, P , D , slip rate, and dip were all varied in grid searches. These models prefer a more strongly locked zone from ~ 5 – 16 km depth on a shallowly dipping ($\sim 35^\circ$) fault slipping ~ 10 – 12 mm/year.

stress-shadow effect updip of the locked portion of subduction megathrusts that should prevent significant creep on the unlocked updip portion of the fault regardless of its frictional stability (Almeida et al., 2018). In other words, even an unlocked, frictionally stable shallow portion of a megathrust may not feel high enough driving stresses to creep interseismically when located updip of a strongly locked patch. By analogy, this type of model may predict that significant shallow creep updip of a more strongly locked portion of a LANF should not occur, either.

Because the downdip width (~19 km) of the locked LANF patch inferred by model 2 is much smaller than that of a locked megathrust, and because along-strike locking patterns may be heterogeneous and patchy, the efficacy of this stress shadow effect may be limited. Additionally, the stress shadow models (Almeida et al., 2018) assume homogeneous elastic properties at all depths, whereas the shallow portions of many normal fault hanging walls consist of unconsolidated, fractured sedimentary units. High shear stresses associated with deep creep between strong metabasaltic and plutonic rocks could be expected to drive more internal deformation and/or fault creep in weak hanging wall sediments at shallow levels than in the strong hanging wall of the homogeneous model. Heterogeneous locking and elastic properties along with frictionally weak, velocity-strengthening shallow fault gouges (section 3) help explain how shallow interseismic creep coeval with deeper locking (model 2) is a mechanically feasible model for interseismic LANF slip.

3. Mai'iu Fault Frictional Strength and Stability From Rock Deformation Experiments

3.1. Fault Rock Sample Descriptions

Over three field seasons, spectacular exposures of the Mai'iu fault were observed and sampled. Structural results show that fault slip has occurred primarily within fault rocks comprising a narrow (<3 m), high strain fault core (Little et al., 2019) (Figure 5). The frictional properties of these fault rocks likely govern the mode of frictional fault slip at different levels on the fault. Figure 5b shows a schematic section of the Mai'iu fault rock sequence that is partially eroded on exhumed parts of the active fault, but fully preserved in outcrops along the inactive segment of the Mai'iu fault. Eight Mai'iu fault rock samples were studied in detail to determine their mineralogy and frictional properties: two types of footwall foliated cataclasite (Figure 5c); a footwall ultracataclasite (Figure 5d); four types of footwall fault gouge (Figures 5e and 5f); and a sliver of hanging wall serpentinite schist entrained within the footwall (Figure 5c, inset).

The mylonitic rocks (not sampled for friction experiments) were overprinted and reworked into the structurally overlying, ~2 m-thick foliated cataclasites. The latter contains veins of friction melt (pseudotachylite), brittle faults, and multiple generations of calcite veins (Figure 5c). The foliated cataclasites investigated in this study (PNG16-17-D2H and PNG16-151E) have a cm-to-mm-spaced, differentiated, and pervasively folded foliation defined by light-colored albite and quartz \pm calcite-rich domains and darker phyllosilicate (predominantly chlorite)-rich folia. This microstructure indicates fluid-assisted diffusive mass transfer during the dissolution of mafic minerals (epidote and actinolite) (Mizera, Little, Boulton, Prior, et al., 2020). Shear-induced creep by diffusive mass transfer and/or frictional viscous flow likely accompanied the formation and folding of the pervasive foliation (Little et al., 2019; Mizera, Little, Boulton, Prior, et al., 2020).

In all outcrops, the foliated cataclasites are overlain sharply by a 5- to 40-cm-thick ultracataclasite (PNG15-50B) formed through cataclastic grain-size reduction and authigenic precipitation of calcite, corrensite, and potassium feldspar (Figure 5d). Massive green-gray and red mafic gouges (PNG14-33A and PNG14-33B) or light (PNG14-19E) to medium gray (PNG14-19F) corrensite-saponite gouges sharply overlie the ultracataclasite layer and form the <20-cm-thick principal slip zone in surface outcrops (Figures 5a, 5b, 5e, and 5f).

3.2. Experimental Methods and Materials

We performed hydrothermal friction experiments on powdered gouges derived from eight of these Mai'iu fault rock types (Figure 6; Tables 1 and S6) using the rotary shear apparatus in the High Pressure and Temperature Laboratory at Utrecht University (Niemeijer et al., 2008, 2016). In these experiments, a thin layer (~1.5 mm) of gouge is placed between two ring-shaped Ni-alloy pistons (22/28 mm inside/outside diameter) and confined by Ni-alloy rings with a low friction (Molykote) coating. The piston assembly is mounted inside a water-filled pressure vessel that houses an internal furnace. The vessel is located within a 100-kN capacity Instron loading frame which is used to apply the normal force. Rotation of the vessel



Figure 5. Summary of fault rocks analyzed. Sample locations are shown in Figures 1e and S7 and listed in Table S6. (a) Exposure of the inactive Mai'iu fault showing the footwall fault rock sequence sharply overlain by unmetamorphosed hanging wall sedimentary rocks. (b) A schematic cross section through the fault core, including the structural position of the fault rocks sampled (after Little et al., 2019; Mizera, Little, Boulton, Prior, et al., 2020). (c) Fault-exhumed exposure of the foliated cataclasite unit and a pseudotachylite vein. Inset: foliated serpentine schist (>10 m thick) entrained between the footwall and hanging wall of the Mai'iu fault, stranded atop the footwall north of Mt. Masasoro. (d) Outcrop of cohesive ultracataclasite unit structurally overlying foliated cataclasites. (e) Mafic fault gouges, and (f) corrensite-saponite fault gouge comprising the principal slip zone.

creating shear within the layer is achieved using an electromotor attached to two 1:100 gear boxes. For more details, refer to Niemeijer et al. (2008, 2016). To create a powdered gouge, samples were crushed and sieved to a grain size fraction $<150\ \mu\text{m}$. In all experiments, we applied stepwise increases in effective normal stress (15 MPa/km), fluid pressure (10 MPa/km), and temperature ($25^\circ\text{C}/\text{km}$) to simulate slip in progressively deeper parts of the fault (Table 1). The temperature gradient imposed was informed by geophysical and geological evidence for a $17\text{--}26^\circ\text{C}/\text{km}$ geothermal gradient on the Mai'i'u fault (Daczko et al., 2009; Little et al., 2019; Martinez et al., 2001; Mizera, Little, Boulton, Biemiller, et al., 2020; Mizera, Little, Boulton, Prior, et al., 2020; Tjhin, 1976). The thermal structure of the Mai'i'u fault is summarized in Little et al. (2019), who document that two exploration wells and shipboard heat flow measurements indicate a present-day geothermal gradient of only $\sim 20^\circ\text{C}/\text{km}$ assuming thermal equilibrium of the temperature measurements and a tropical seafloor temperature of 20°C at $\sim 30\ \text{m}$ depth (Tjhin, 1976). In Goodenough Bay, topography and sediment-corrected heat flow data average $73\ \text{mW}/\text{m}^2$. Assuming a linear geotherm and lithospheric conductivity of $3.2\ \text{W}/\text{m}^\circ\text{C}$, this translates into a geothermal gradient of $\sim 23^\circ\text{C}/\text{km}$ (cf. Martinez et al., 2001). Mizera, Little, Boulton, Prior, et al. (2020) present a geologically constrained thermal profile of the Mai'i'u fault. Temperature in the mylonites is pinned by the pseudosection thermobarometry of Daczko et al. (2009), which revealed a temperature of 425°C at $25\ \text{km}$ depth, which is less than $17^\circ\text{C}/\text{km}$. Additional temperature constraints are provided by the chemistry of syntectonic chlorite in the foliated cataclasites (our samples PNG-16-17-D2H and PNG-16-151e), which yields a temperature range of 158°C to 356°C with an average of $273 \pm 46^\circ\text{C}$ (1σ) (Mizera, Little, Boulton, Prior, et al., 2020). Based on known slip rates and Ar-Ar pseudotachylyte ages, the foliated cataclasites were exhumed from $10\text{--}12\ \text{km}$, yielding a mean geothermal gradient of $\sim 22 \pm 4^\circ\text{C}/\text{km}$ (Little et al., 2019). Clay mineralogy (corrensite and saponite) indicate lower temperatures in fault gouges formed at depths $<10\ \text{km}$, and mylonite chlorite geothermometry indicates higher temperatures at depths $>12\ \text{km}$ (Mizera, Little, Boulton, Biemiller, et al., 2020; Mizera, Little, Boulton, Prior, et al., 2020).

Once the desired pressure (P) and temperature (T) conditions were reached, we allowed the system to equilibrate for at least 30 min before shearing began at $1\ \mu\text{m}/\text{s}$. Initial shearing at $1\ \mu\text{m}/\text{s}$ occurred for 5 mm to establish a steady state friction level and a mature microstructure. The velocity dependence of friction was investigated by subsequently applying a velocity-stepping scheme of $0.3\text{--}1\text{--}3\text{--}10\text{--}30\ \mu\text{m}/\text{s}$. Following these velocity steps, the motor driving displacement was stopped, and PT conditions were changed. Under the new PT-conditions, the $1\ \mu\text{m}/\text{s}$ run-in displacement was reduced to 2.5 mm, but otherwise the procedure remained the same. The frictional properties of each fault rock were measured over a range of temperatures and pressures corresponding to an active, extensional fault zone (Table 1); a more detailed analysis of the pressure and temperature conditions at depth in the Mai'i'u fault zone can be found in Mizera, Little, Boulton, Prior, et al. (2020). Data were acquired at a rate of 900 Hz and averaged to rates of $1\text{--}100\ \text{Hz}$, depending on the sliding velocity. Raw data were processed to obtain shear stress as a function of sliding distance, which was further analyzed in terms of rate-and-state frictional properties using a Dieterich state evolution law (Dieterich, 1979, 1981; Marone, 1998) and the inversion scheme detailed in Reinen and Weeks (1993) and Ikari et al. (2009) (Text S6).

Although increasing temperature, normal stress, and fluid pressure in tandem makes it difficult to isolate the effects of each individual condition, this step-wise simulated-depth approach allowed for finer sampling of the suite of depth-dependent crustal conditions under which each sampled fault rock unit is inferred to have deformed in the natural fault zone. We note that future experiments on the exhumed Mai'i'u fault rock sequence testing a range of each individual experimental condition (e.g., experiments at different temperatures under identical fluid pressures and effective normal stresses) could be used to isolate and quantify the individual effects of temperature, fluid pressure, and normal stress and allow these results to be more broadly applied to other mature mafic fault zones with different geothermal gradients or fluid pressure distributions. Nonetheless, the range of depths simulated by the experimental conditions here (Table 1) provide a detailed account of the depth-dependent mechanical behavior of the Mai'i'u fault (Figures 6–8).

3.3. Frictional Strength Results

We report the results of all experiments in Figure 6, which shows the coefficient of friction (defined as shear stress/effective normal stress, ignoring cohesion) as a function of load-point displacement. All samples tested show changes in friction with PT conditions, but the largest differences in friction are between samples. The

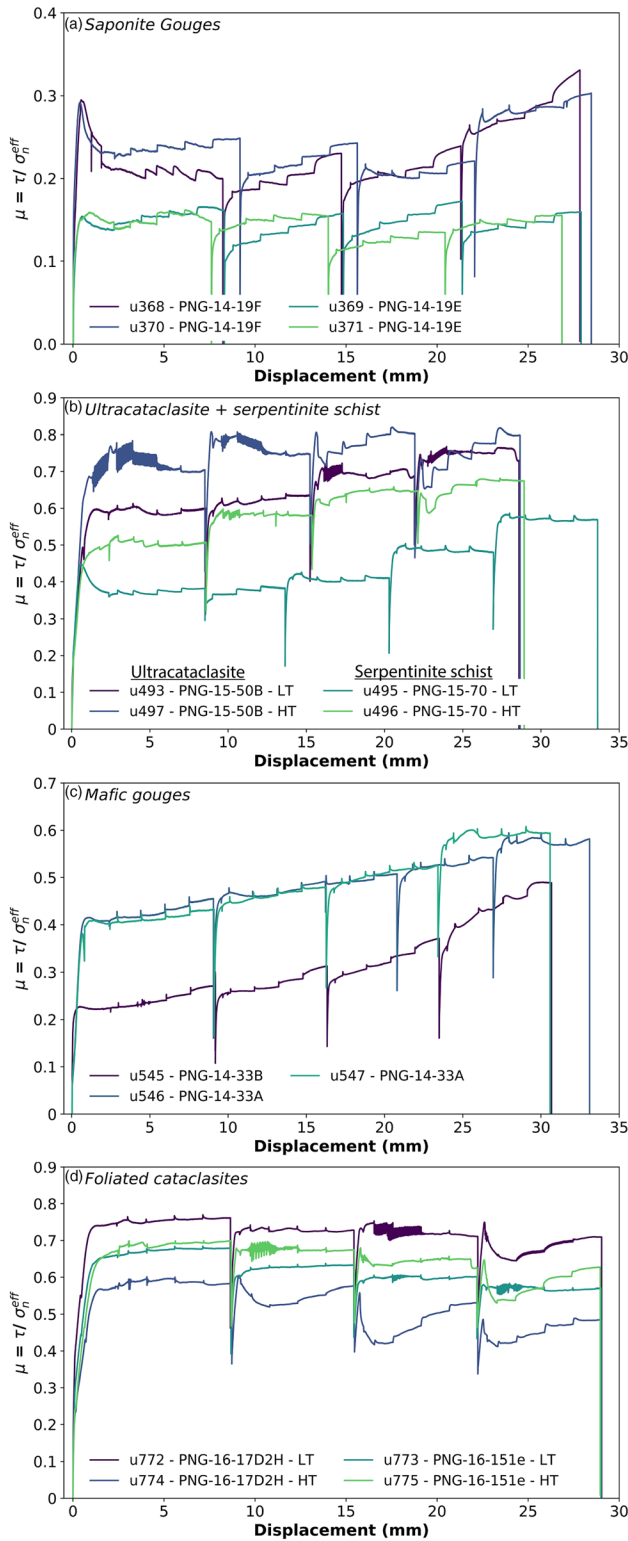


Figure 6. Friction measured during velocity-step experiments on Mai'iu fault rocks (section 3.1, Figure 5, Tables S6–S7) including (a) corrensite-saponite gouges; (b) ultracataclasite and serpentinite schist; (c) mafic gouges; (d) foliated cataclasites. Colors indicate individual experiments (“u368”) on numbered samples (“PNG-14-19F”) under lower-temperature (LT) or higher-temperature (HT) conditions.

measured frictional strength covers the range of $\mu = 0.1$ to $\mu = 0.8$ (see also Table 1 and Text S5). The uppermost, light gray saponite gouge sample is the weakest with $\mu = 0.11$ – 0.15 , followed by the underlying, medium gray saponite gouge ($\mu = 0.18$ – 0.28), the red mafic gouge ($\mu = 0.22$ – 0.35), the serpentinite schist ($\mu = 0.37$ – 0.63), the green-gray mafic gouge ($\mu = 0.40$ – 0.57), the “inactive” foliated cataclasite (0.44 – 0.75), the “active” foliated cataclasite ($\mu = 0.57$ – 0.67), and finally the ultracataclasite ($\mu = 0.59$ – 0.80). The abundance of the weak clay mineral saponite is a good indicator of the weakness of the sample (e.g., Lockner et al., 2011; Sone et al., 2012), whereas the sample derived from the serpentinite schists show friction values in the range of pure lizardite (e.g., Moore et al., 1997; Moore & Lockner, 2013). Friction of the foliated cataclasites and the ultracataclasite is comparable to results from friction studies on gouges of granitic composition (e.g., Niemeijer et al., 2016), of quartz (e.g., Chester & Higgs, 1992; Niemeijer et al., 2008), and of plagioclase (e.g., He et al., 2013). In general, the friction coefficients of most fault gouges increase with increasing simulated depth (i.e., increasing temperature, effective normal stress, and fluid pressure) during an individual experiment. In some experiments, strengthening is the result of a long-term displacement-dependent increase in friction (e.g., Figure 6c), whereas in other experiments strengthening is abrupt and is the result of increased simulated depth (e.g., Figure 6b).

3.4. Rate-and-State Frictional Stability Results

Although a relationship between fault strength and frictional stability has been proposed (Ikari et al., 2011), fault frictional strength alone gives little indication as to whether the fault creeps aseismically or slips in episodic earthquakes. Instead, frictional stability is described within the framework of rate-and-state friction, where the instantaneous effective friction coefficient depends on both the current slip velocity (“rate”) and the time over which two fault surfaces have been in contact with each other (“state”). Experimentally derived values of rate-state parameters a , b , and critical slip distance d_c describe the frictional stability of a material: materials with $(a-b) > 0$ are velocity-strengthening, whereby an increase in slip velocity causes an increase in friction promoting stable creep; materials with $(a-b) < 0$ are velocity-weakening, whereby an increase in slip velocity causes a decrease in friction, promoting unstable, potentially seismic slip (e.g., Dieterich, 1979, 1981; Gu et al., 1984; Rice & Tse, 1986; Ruina, 1983).

We invert the velocity-stepping data for individual rate-state friction parameters a , b , and d_c . Figure 7 shows $(a-b)$ values as a function of up-step sliding velocity for all samples tested. There is considerable variation in $(a-b)$ with simulated depth. All samples show some negative $(a-b)$ values under certain experimental conditions, indicating potential for unstable slip. In all fault gouge-derived samples, $(a-b)$ increases with increasing sliding velocity, regardless of the depth simulated (Figures 7a and 7c). Negative values are restricted to temperatures of 150–200°C. Samples derived from foliated cataclasites and ultracataclasites show predominantly negative values of $(a-b)$ transitioning to positive values at temperatures of 400 and 450°C. Interestingly, at $T = 400$ and 450°C , the cataclasites’ $(a-b)$ decreases with increasing sliding velocity. Finally, $(a-b)$ values for the sample derived from serpentinite schist show three regimes of velocity dependence: lower temperature (150°C) velocity

Table 1

List of Sampled Fault Rocks and Experiments Performed With Experimental Conditions (Effective Normal Stress, Pore Fluid Pressure, and Temperature) and Values of Friction (=Shear Stress/Effective Normal Stress, Ignoring Cohesion) at the End of Each Run-In (at 1 mm/s)

Exp.	Sample #	Fault rock	σ_n^{eff} (MPa)	P_f (MPa)	T (°C)	μ_{ss}
u368 ^a	PNG-14-19F	Lower gouge	30-60-90-120	20-40-60-80	50-100-150-200	0.24-0.18-0.19-0.26
u369 ^a	PNG-14-19E	Upper gouge	30-60-90-120	20-40-60-80	50-100-150-200	0.14-0.11-0.13-0.13
u370	PNG-14-19F	Lower gouge	30-60-90-120	20-40-60-80	50-100-150-200	0.23-0.21-0.20-0.28
u371	PNG-14-19E	Upper gouge	30-60-90-120	20-40-60-80	50-100-150-200	0.15-0.13-0.11-0.14
u487	PNG-15-50B ^b	Ultracataclasite	120-150	80-100	200-250	0.63-0.74
u493	PNG-15-50B	Ultracataclasite	90-120-150-180	90-120-150-180	150-200-250-300	0.59-0.59-0.66-0.72
u495	PNG-15-70	Serpentinite	90-120-150-180	90-120-150-180	150-200-250-300	0.37-0.41-0.48-0.57
u496	PNG-15-70	Serpentinite	120-150-180-210	80-100-120-140	300-350-400-450	0.50-0.60-0.62-0.63
u497	PNG-15-50B	Ultracataclasite	120-150-180-210	80-100-120-140	300-350-400-450	0.75 ^c -0.80-0.80-0.73
u545	PNG-14-33B	Upper mafic gouge	30-60-90-120	20-40-60-80	50-100-150-200	0.22-0.26-0.28-0.35
u546	PNG-14-33A	Lower mafic gouge	30-60-90-120	20-40-60-80	50-100-150-200	0.41-0.46-0.50-0.56
u547	PNG-14-33A	Lower mafic gouge	30-60-90-120	20-40-60-80	50-100-150-200	0.40-0.44-0.48-0.57
u772	PNG-16-17D2H	Foliated cataclasite	90-120-150-180	60-80-100-120	150-200-250-300	0.75-0.72-0.73-0.72 ^c
u773	PNG-16-151e	Foliated cataclasite	90-120-150-180	60-80-100-120	150-200-250-300	0.66-0.60-0.59-0.57
u774	PNG-16-17D2H	Foliated cataclasite	120-150-180-210	80-100-120-140	300-350-400-450	0.57-0.60-0.47-0.44
u775	PNG-16-151e	Foliated cataclasite	120-150-180-210	80-100-120-140	300-350-400-450	0.67-0.67-0.66 ^c -0.61

Note. The sliding velocity was 1 mm/s initially and then stepped to 0.3-1-3-10-30 mm/s with 0.5-1.5-1.5-1.5-1.5 mm of displacement. Steady state friction (μ_{ss}) is determined at the end of the run-in at 1 mm/s at each σ_n^{eff} -T- P_f condition.

^aRun-in at 10 mm/s, step from 0.3 to 1 mm/s omitted, step from 30–100 mm/s included. ^bExperiment terminated prematurely due to pore fluid leak.

^cIndicates peak value of stick-slip.

strengthening, intermediate temperature (200–350°C) velocity weakening, and high temperature velocity strengthening (400–450°C). As before, (*a-b*) decreases with increasing sliding velocity in the higher-temperature regime. The serpentinite schist's rate dependence is consistent with the behavior of lizardite, a low-temperature ($T < 300^\circ\text{C}$) serpentine mineral that comprises 82% of the sample (e.g., Moore et al., 1997; Moore & Lockner, 2013; Schwartz et al., 2013) (Table S6).

4. Discussion

4.1. Experimental Constraints on Fault Slip Behavior

4.1.1. Evidence for Frictional Strain-Weakening of a Rolling-Hinge Detachment

Our experimental results show that the Mai'iu fault gouges inferred to be active at the shallowest depths are frictionally weak ($\mu = 0.11\text{--}0.35$), with the most phyllosilicate-rich (saponitic) gouge exhibiting the lowest static friction coefficients of 0.11–0.15. Saponite is thermodynamically unstable above $\sim 150^\circ\text{C}$ (e.g., Boulton et al., 2018; Moore, 2014), implying that these weak gouges control the frictional strength of only the shallowest and most mechanically misaligned portions of the Mai'iu fault, down to inferred depths of ~ 6 km (Figure 8; Mizera, Little, Boulton, Prior, et al., 2020). At greater depths and higher temperatures ($T = 150\text{--}225$ and $150\text{--}300^\circ\text{C}$, respectively), chlorite thermometry from syntectonic structures (e.g., veins, shear bands) indicates that slip occurred in the mafic ultracataclasite and foliated cataclasite units (Mizera, Little, Boulton, Prior, et al., 2020), which are frictionally stronger ($\mu = 0.59\text{--}0.80$ and $\mu = 0.44\text{--}0.75$, respectively). This increase in frictional strength with depth coincides with the depth range over which the fault dip steepens from $15\text{--}22^\circ$ in the upper 4–5 km to $30\text{--}40^\circ$ below 5–6 km (Abers et al., 2016; Little et al., 2019; Mizera et al., 2019; Webber et al., 2020). Based on this striking correlation between fault dip at depth and the static frictional strength of the associated fault rocks deformed at those depths, we infer that the static frictional strength of the Mai'iu fault rocks partially controls the fault geometry, with slip at shallow dip angles in the near-surface facilitated by abundant weak saponitic gouges, and slip at steeper dip angles at greater depths occurring on frictionally stronger (ultra-)cataclasites. Formation of saponite (or other weak phyllosilicate minerals in other LANFs) results in a synexhumational reaction-weakening of the fault, consistent with classic geodynamic models of detachment faults that require plastic strain-weakening of the normal fault zone in order for it to evolve into a long-lived rolling hinge-style detachment (e.g., Lavier et al., 1999, 2000). Although this geodynamic plastic strain-weakening is commonly modeled as a loss of cohesion (e.g., Choi & Buck, 2012; Choi et al., 2013; Lavier et al., 1999, 2000), our experimental results show that the effective strain-weakening of an active rolling-hinge detachment fault (Little et al., 2019; Mizera

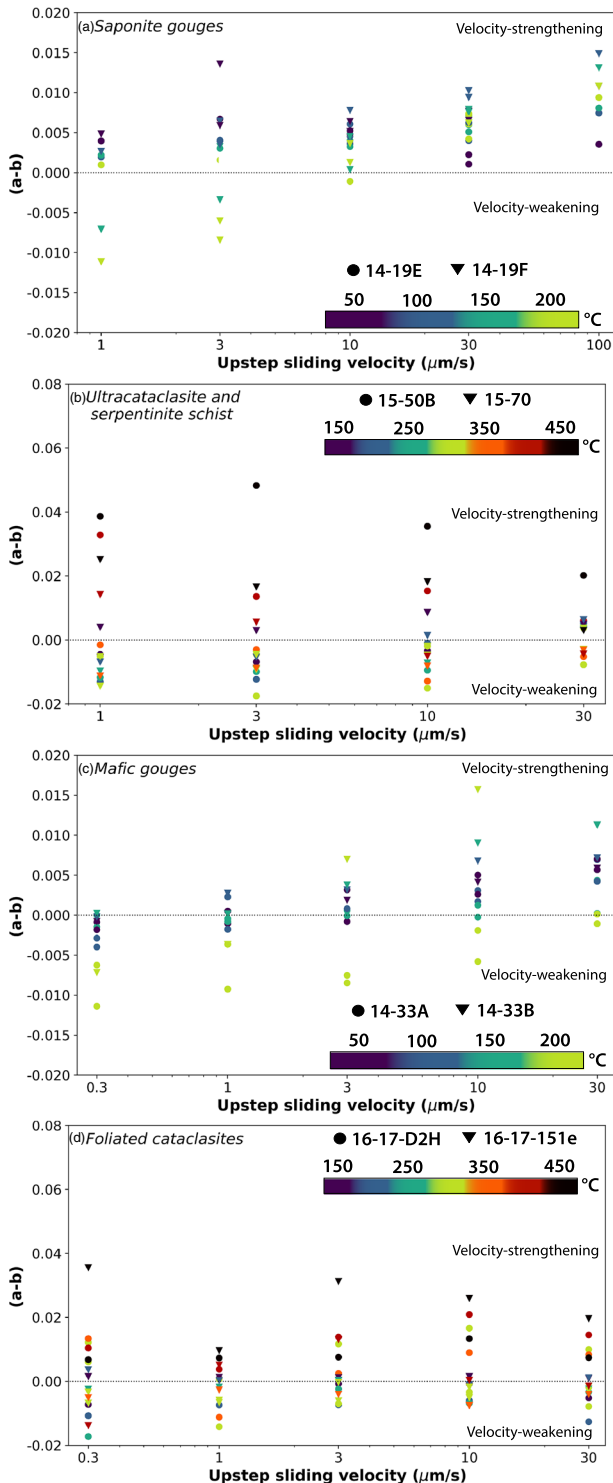


Figure 7. Rate-state-friction stability parameters ($a-b$) from velocity-stepping experiments on Mai'iu fault rocks (section 3.1, Figure 5, Tables S6–S7) including (a) corrensite-saponite gouges; (b) ultracataclasite and serpentinite schist; (c) mafic gouges; (d) foliated cataclasites.

The fault rocks active at greater depths ($> \sim 6$ km, based on temperatures $> 150^\circ\text{C}$ from Mizera, Little, Boulton, Prior, et al., 2020) are more strongly and consistently velocity-weakening than any of the shallowly formed gouges. The cataclasites and ultracataclasite samples show predominantly negative ($a-b$) values

et al., 2019) can be at least partially accomplished by the reduction of the static coefficient of friction as a result of fluid-assisted mineral transformation reactions that form weak phyllosilicate minerals such as saponite.

The static frictional strength of active LANFs is thought to influence both fault geometry according to classical Mohr-Coulomb-type fault mechanics (e.g., Axen, 2004; Choi & Buck, 2012; Choi et al., 2013; Collettini & Sibson, 2001; Collettini, Viti, et al., 2009; Yuan et al., 2020) and wedge geometry according to critical wedge theory and limit analysis (e.g., Yuan et al., 2020). The low frictional strength ($\mu \sim 0.2$) of clay-rich and/or hydrated gouge minerals such as talc and smectite should allow normal faults filled with these minerals to remain active at shallower dips (e.g., Collettini, 2011) and may resolve the apparent mechanical paradox of these anomalously low-angle structures. Although prior experimental friction studies of LANF zone rocks show some evidence of friction coefficients of 0.2–0.3 in the most phyllosilicate-rich or heavily foliated samples, many previously tested gouges show friction coefficients > 0.4 (Collettini, Viti, et al., 2009; Haines et al., 2014; Niemeijer & Collettini, 2014; Numelin, Marone, & Kirby, 2007; Smith & Faulkner, 2010). Our results confirm that shallow LANF gouges can be extremely frictionally weak, but suggest that LANF strength at greater depths depends on the frictional strength of the deeper fault rock protoliths of these gouges.

4.1.2. Depth-Dependent Frictional Stability

One explanation for the paucity of recorded earthquakes on some LANFs is that they primarily creep aseismically (e.g., Abers, 2009; Hreinsdóttir & Bennett, 2009), implying that the fault material is predominantly velocity-strengthening through the brittle crust (e.g., Collettini, 2011). Indeed, velocity-stepping experiments on exhumed LANF gouges (Niemeijer & Collettini, 2014; Numelin, Marone, & Kirby, 2007; Smith & Faulkner, 2010) and typical LANF gouge minerals (Collettini, 2011, and references within) show predominantly velocity-strengthening behavior under upper crustal conditions, with a thermally activated transition to velocity-weakening behavior at $> 300^\circ\text{C}$ (Niemeijer & Collettini, 2014).

Velocity-stepping experiments on Mai'iu fault sequence rocks ranging from mylonitic protoliths to well-developed gouges were performed under a range of temperature (50–450°C), effective normal stress (30–210 MPa), and pore-fluid pressure (20–140 MPa) conditions associated with a range of crustal depths (~ 3 –25 km, as inferred by Mizera et al., 2019). The saponite-rich gouges exhibit strictly velocity-strengthening behavior for temperatures $< 150^\circ\text{C}$, with the less-saponitic sample transitioning to velocity-weakening at $T \geq 150^\circ\text{C}$. In contrast, mild velocity-weakening behavior is observed for low upstep-velocities at $T = 50$ – 200°C in the mafic gouges, which contain less saponite ($< 22\%$) and more remnant (ultra-)mafic clasts, chlorite, actinolite, and epidote. The mafic gouges transition to velocity-strengthening with increasing upstep-velocity. These results suggest that the Mai'iu fault likely creeps at $T < 150^\circ\text{C}$ ($< \sim 6$ km depth), but that local fault stability depends on the proportion of saponite to mafic components in the gouge. The hydrological and thermochemical conditions that promote the formation and accumulation of saponite appear crucial to development of frictionally weak, velocity-strengthening behavior in the upper reaches of the fault zone.

($-0.02 < (a-b) < 0$) at 150–350°C, transitioning to consistently positive ($a-b$) values ($0 < (a-b) < 0.05$) at $\geq 400^\circ\text{C}$. This transition to velocity-strengthening behavior around $T = 400^\circ\text{C}$ corresponds to the conditions under which most chlorite and chlorite-actinolite gouges have been observed to be strongly velocity-strengthening ($T \geq 400^\circ\text{C}$ and $\sigma_n^{\text{eff}} = P_f \geq 100$ MPa, Okamoto et al., 2019, 2020). We infer that deformation at depths greater than the $\sim 400^\circ\text{C}$ isotherm ($> \sim 20$ –25 km depth) occurs primarily by aseismic ductile creep in the mafic mineral assemblage (chlorite, actinolite) within the mylonitic shear zone.

Altogether, the experimental friction results outline three primary temperature-dependent stability regimes of the Mai'iu fault rock sequence: low-temperature ($\leq 150^\circ\text{C}$) velocity-strengthening, intermediate-temperature (150–350°C) velocity-weakening, and high-temperature velocity-strengthening (400–450°C). Because the driving velocity in our experiments (1 $\mu\text{m/s}$) is orders of magnitude faster than natural tectonic plate rates, the frictional stability transitions observed in each rock type may shift to somewhat lower temperatures at slower deformation rates, as predicted by microphysical models (e.g., Chen et al., 2017, and references therein). In addition, laboratory experiments and geological mapping cannot constrain the size and spatial distribution of frictionally locked patches, which are determined by a variety of factors including the spatial distribution of different fault rocks and gouge minerals, local thermal structure, fault roughness and architectural complexity, presence and distribution of pore fluids, and local history and heterogeneity of stress and slip on the fault, among others (e.g., Avouac, 2015; Bürgmann, 2018; Harris, 2017; Scholz, 2019; references within).

4.2. Contemporary Slip Behavior in the Context of Geological and Experimental Evidence

GPS velocities near the active Mai'iu LNF reveal ~ 8 mm/year of horizontal extension corresponding to ~ 10 mm/year dip-slip on a normal fault dipping 26–35°. Horizontal velocities are fit similarly well by ~ 10 mm/year of dip-slip with distinctly different distributions of interseismic fault locking: (1) aseismic creep below a shallowly locked patch (~ 2 km deep) that projects to the surface at the main fault trace; or (2) aseismic creep updip and downdip of a deeper locked patch (locked from ~ 5 –16 km depth) that projects to the surface along a splay fault within the hanging wall. We evaluate these two scenarios with respect to the experimental friction results alongside geological and geophysical evidence of Mai'iu fault slip.

The strongly velocity-strengthening behavior of the shallowest saponitic Mai'iu fault gouges (Figure 7a) suggests frictionally stable creep near the surface, while the predominantly velocity-weakening behavior of the cataclastic fault units deformed at greater depths (Figures 7b and 7d) points to deeper seismic slip and interseismic locking. The largely velocity-weakening behavior of the cataclasites and ultracataclasites from $T = 150$ –350°C implies that frictional fault slip from ~ 8 –20 km depth likely occurs as seismic or microseismic events that release elastic strain accumulated around frictionally locked patches. Along with evidence for sufficient seismic slip to generate pseudotachylite melts at 10–12 km depth (Little et al., 2019) and cause episodic meter-scale coastal uplifts further along-strike as recorded by emerged fossilized coral reefs (section 1.2; Biemiller et al., 2018), these results are most consistent with model 2 (Figures 3d–3f), which exhibits strong locking over the ~ 5 –16 km depth range and would predict both earthquake nucleation and relatively uninhibited earthquake propagation through frictionally unstable velocity-weakening fault rocks (Figures 6–8). Model 1, by contrast, predicts aseismic creep below 2 km depth and negligible seismogenic potential at the depths of pseudotachylite formation and velocity weakening fault rocks. Although seismic rupture nucleated elsewhere could potentially propagate through a creeping segment to generate pseudotachylites, the depth-dependent stratification of fault slip stability illustrated by experimental friction and microstructural evidence implies deeper, stronger locking most consistent with model 2.

Frequent and localized microseismicity is common along actively creeping fault segments (e.g., Bürgmann et al., 2000; Harris, 2017; Malservisi et al., 2005; Wolfson-Schwehr & Boettcher, 2019). Strongly aligned microseismicity from ~ 12 –25 km depth (Figure 1d; Abers et al., 2016) not only outlines the deeper extent of the Mai'iu fault, but also suggests that a deeper portion of the fault zone actively creeps, generating microseismic events during frictional failure of small locked asperities within the creeping shear zone. The updip cutoff depth of this microseismicity suggests a transition from steady creep below to stronger locking above, and may be associated with a transition from frictional-viscous velocity-strengthening creep to frictional velocity-weakening behavior around 10–15 km (Figure 8); however, because the Mai'iu fault is near the edge of the seismic network of Abers et al. (2016), the exact depth of this transition as defined by microseismicity is not tightly constrained (Figure 1d). It is also important to note that the network of permanent continuous

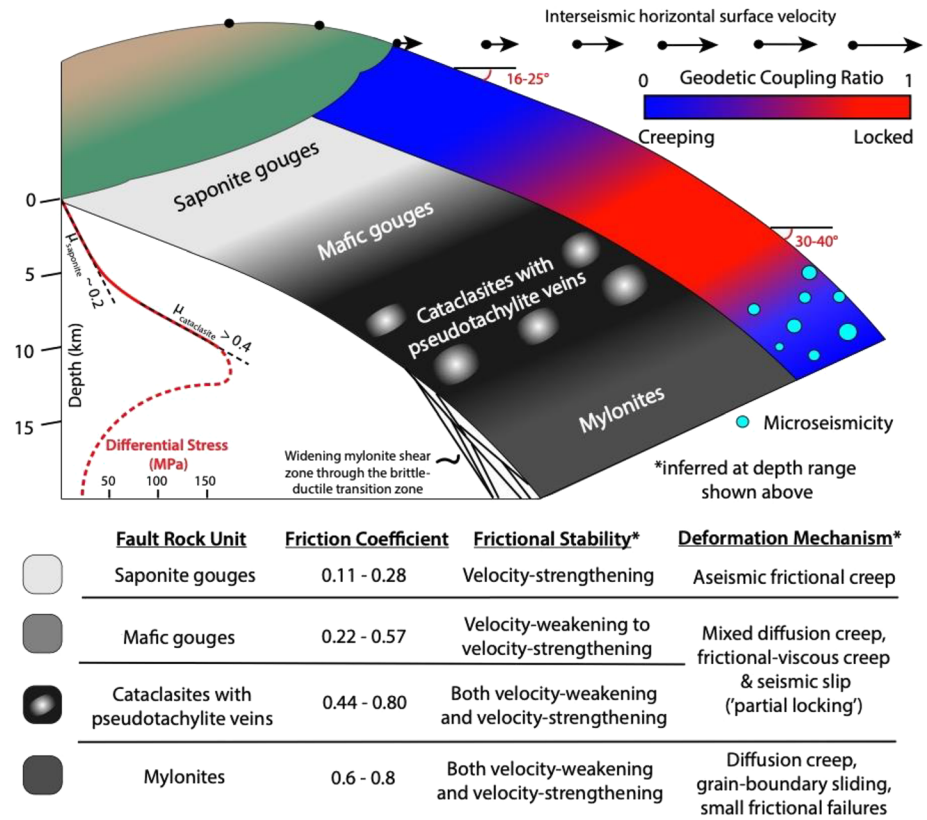


Figure 8. Inferred distribution of active Mai'iu fault rocks and deformation mechanisms, along with the resulting geodetic coupling and horizontal surface velocities. Stronger locking occurs in the velocity-weakening cataclastic units, while stable interseismic creep occurs updip and downdip of this zone in the saponite gouges and mylonites, respectively. Frictional stability and strength derived from experiments (Figures 6–7) for all units except the mylonites, for which frictional behavior is inferred from microstructures (Little et al., 2019; Mizera, Little, Boulton, Prior, et al., 2020) and microseismicity (Abers et al., 2016). The differential stress profile is based on frictional strength above the brittle-ductile transition zone (solid line) and inferred only schematically below (dashed line), but is consistent with preliminary peak differential stress estimates of ~140–185 MPa in the cataclasites from calcite twinning geopiezometry (Mizera, Little, Boulton, Biemiller, et al., 2020).

seismometers in PNG is sparse and that dense deployments (e.g., Abers et al., 2016; Ferris et al., 2006) have thus far been temporary; hence, the detection limit for earthquakes near the Mai'iu fault is high ($M_w > 4-5$) and it is typically not possible to compute high-quality locations for these events, making it difficult to detect and identify any potential seismic indicators of slip behavior such as small ($M_w < 4$) repeating earthquakes adjacent to strongly locked patches. We suggest that future work involving dense permanent or semipermanent seismic deployments focused on the Mai'iu fault could reveal even more details of active LANF mechanics and, in particular, more tightly constrain the spatial distribution of locked, creeping, and partially coupled portions of the Mai'iu fault.

The apparent seismically delineated depth-dependent mechanical transitions on the Mai'iu fault may be explained by our experimentally observed frictional transition from velocity-weakening to velocity-strengthening behavior in the cataclastic fault rocks at around 400°C (Figures 6–7), as well as the microstructurally recorded mixed frictional-viscous deformation in the cataclasites and mylonites (Little et al., 2019; Mizera, Little, Boulton, Prior, et al., 2020). The general depth range of this mechanical transition agrees well with model 2's predicted coupling transition from stronger locking around 5–16 km depth to creep downdip of this region; this coupling transition is not predicted by model 1 (Figures 3 and 8). Combining our geodetic results with the diverse geological, experimental, and seismological evidence for mixed seismic slip and aseismic creep, we infer that the Mai'iu fault is more strongly locked and potentially seismogenic from ~5–16 km depth and creeps both updip and downdip of this zone (model 2; Figure 8).

4.3. Mechanical Implications for LANFs

Active aseismic LANF creep below a shallow locking depth (model 1) would agree well with previous geodetic inferences of shallow aseismic creep on another active LANF, the Altotiberina fault (Hreinsdóttir & Bennett, 2009). However, allowing for more complex structures including creep and locking of nearby splay faults, subsequent modeling of the Altotiberina fault (Anderlini et al., 2016) has shown that a spatially heterogeneous pattern of locked and creeping patches is more consistent with observed surface GPS velocities. Similarly, based on the velocity-weakening frictional behavior of exhumed fault rocks, coseismically generated pseudotachylites exhumed from ~10–12 km depth, microseismicity data highlighting fault creep below ~12 km depth, and the results of geodetic models that allow for splay fault slip and patchy locking at depth, the Mai'iu fault appears to be more strongly locked from ~5–16 km depth (model 2) and to be creeping interseismically along its shallowest portions (<~5 km depth).

We suggest that the strongly coupled depth range of ~5–16 km corresponds to the brittle strength peak for the Mai'iu fault rock sequence where interseismic elastic strain can accumulate between periods of cataclastic deformation of potentially unstable velocity-weakening mylonitic protoliths (i.e., cataclasite and ultracataclasite units, Figures 5–7). With progressive slip and exhumation, fluid-assisted chemical reactions precipitate frictionally stable velocity-strengthening phyllosilicate gouge minerals (clays such as saponite; Figure 7a), responsible for the apparent transition toward aseismic creep near the surface. Models with deep locking below ~15 km do not fit the GPS data well (Figures 4, S4, and S6); therefore, we infer that downdip of the strongly locked portion, slip occurs mostly by aseismic diffusive mass transfer creep processes, punctuated by microseismicity associated with occasional failure of small locked asperities and the fracturing of intact competent clasts within the primarily ductilely deforming shear zone and also by the infrequent downdip propagation of large earthquake slip. While we propose that the apparent depth-dependence of Mai'iu fault slip behavior is related to depth-aligned syn-extensional transitions in fault rock mineralogy, it is important to note that many physical conditions besides mineralogy also vary with depth. Thus, the inferred stratification of fault slip behavior likely results from intertwined transitions in temperature, fluid pressure, and mineralogy. Transitions from aseismic locked patches to microseismic creeping patches are common along strike-slip faults (e.g., Avouac, 2015; Bürgmann, 2018; Harris, 2017; references within). Along subduction megathrusts, lithology-dependent transitions in rheological and frictional properties (e.g., Behr et al., 2018) may explain the downdip transition from locked to slow-slipping/creeping regions with microseismicity and/or tremor (e.g., Bostock et al., 2019; Lay et al., 2012; Schwartz & Rokosky, 2007).

Our preferred interpretation of slip on the Mai'iu fault implies that it may be capable of hosting and even nucleating sizeable, albeit relatively infrequent, earthquakes. Assuming a typical dip-slip rupture width-length ratio of 0.668 (Leonard, 2010) and shear modulus of 25 GPa, nominal slip of 1 m on a locked patch dipping 35° from 5–16 km depth would correspond to a ~ M_w 6.7 earthquake; allowing for rupture to the surface increases this estimate to ~ M_w 7.0. These estimated magnitudes agree well with both the largest reported LANF earthquake globally (M_w 6.8, 29 October 1985; Abers, 1991; Abers et al., 1997) and estimations of Mai'iu fault earthquake magnitude based on the stress and slip required for coseismic melting and pseudotachylite formation (M_w 6.0+; Little et al., 2019). Taken together, these observations and calculations illustrate the potential severity of Mai'iu fault earthquakes and the importance of including the Mai'iu fault and other active LANFs in future seismic hazard assessments and risk mitigation plans.

5. Conclusions

New campaign GPS and experimental friction data from the Mai'iu fault in PNG illuminate the patterns and mechanisms of creep and locking on one of the world's fastest-slipping, active LANFs. Horizontal GPS velocities indicate 8.3 ± 1.2 mm/year of active extension across the Mai'iu fault. Friction experiments show that clay-rich gouges from the shallowest and most poorly aligned portion of the fault are both weak ($\mu = 0.11$ – 0.35) and predominantly velocity-strengthening, while cataclastic fault rocks deformed at greater depths on more steeply dipping parts of the fault are stronger ($\mu = 0.44$ – 0.84) and predominantly velocity-weakening. Two distinct fault locking models fit the GPS data equally well: one that requires aseismic creep below ~2 km depth and one with a locked patch from ~5–16 km depth. A range of geological, experimental, and seismological data support the geodetic model with interseismic locking from ~5–16 km depth and shallower aseismic creep on the Mai'iu fault and one or more hanging wall splay faults. This model also

agrees with geological and coral paleoseismological evidence of seismic slip on the Mai'u fault and confirms that LANFs may be capable of hosting M_w 7.0 + earthquakes despite the abundance of velocity-strengthening fault gouges at shallow depths which promote interseismic creep near the Earth's surface.

Data Availability Statement

Experimental friction data and GPS velocities are given in the supporting information. GPS data are available through the UNAVCO data portal (<https://doi.org/10.7283/BHJ8-4J66>). Experimental friction data are available through the YODA online repository of the Utrecht University (<https://geo.yoda.uu.nl>, as <https://doi.org/10.24416/UU01-7GJW0G>).

Acknowledgments

We first and foremost thank the people of Milne Bay and Oro provinces in Papua New Guinea for their support and hospitality, without which the field-based components would not have been possible. We thank Samuel Webber, Neville Palmer, and Rory Hart for field and technical support. We thank Samuel Webber, Jürgen Österle, Daniel Stockli, Kevin Norton, and Whitney Behr for helpful discussions. This study was supported by the US National Science Foundation grant EAR-1524729 (L.W., L.L., J.B.) and graduate student fellowship program (J.B.), New Zealand Royal Society Marsden Fund grant VUW1310 (T.L., C.B., M.M., S.E.), European Research Council grant SEISMIC (335915) (A.N.), and the Dutch Research Council VIDI grant 854.12.011 (A.N.).

References

- Abers, G. A. (1991). Possible seismogenic shallow-dipping normal faults in the Woodlark-D'Entrecasteaux extensional province, Papua New Guinea. *Geology*, *19*(12), 1205–1208. [https://doi.org/10.1130/0091-7613\(1991\)019<1205:pssdnf>2.3.co;2](https://doi.org/10.1130/0091-7613(1991)019<1205:pssdnf>2.3.co;2)
- Abers, G. A. (2001). Evidence for seismogenic normal faults at shallow dips in continental rifts. *Geological Society, London, Special Publications*, *187*(1), 305–318. <https://doi.org/10.1144/GSL.SP.2001.187.01.15>
- Abers, G. A. (2009). Slip on shallow-dipping normal faults. *Geology*, *37*, 767–768. <https://doi.org/10.1130/focus082009.1>
- Abers, G. A., Eilon, Z., Gaherty, J. B., Jin, G., Kim, Y., Obrebski, M., & Dieck, C. (2016). Southeast Papuan crustal tectonics: Imaging extension and buoyancy of an active rift. *Journal of Geophysical Research: Solid Earth*, *121*, 951–971. <https://doi.org/10.1002/2015JB012621>
- Abers, G. A., Mutter, C. Z., & Fang, J. (1997). Shallow dips of normal faults during rapid extension: Earthquakes in the Woodlark-D'Entrecasteaux rift system, Papua New Guinea. *Journal of Geophysical Research*, *102*(B7), 15,301–15,317. <https://doi.org/10.1029/97jb00787>
- Almeida, R., Lindsey, E. O., Bradley, K., Hubbard, J., Mallick, R., & Hill, E. M. (2018). Can the updip limit of frictional locking on megathrusts be detected geodetically? Quantifying the effect of stress shadows on near-trench coupling. *Geophysical Research Letters*, *45*, 4754–4763. <https://doi.org/10.1029/2018GL077785>
- Anderlini, L., Serpelloni, E., & Belardinelli, M. E. (2016). Creep and locking of a low-angle normal fault: Insights from the Altotiberina fault in the northern Apennines (Italy). *Geophysical Research Letters*, *43*, 4321–4329. <https://doi.org/10.1002/2016GL068604>
- Anzidei, M., Boschi, E., Cannelli, V., Devoti, R., Esposito, A., Galvani, A., et al. (2009). Coseismic deformation of the destructive April 6, 2009 L'Aquila earthquake (central Italy) from GPS data. *Geophysical Research Letters*, *36*, L17307. <https://doi.org/10.1029/2009GL039145>
- Araki, E., Saffer, D. M., Kopf, A. J., Wallace, L. M., Kimura, T., Machida, Y., et al. (2017). Recurring and triggered slow-slip events near the trench at the Nankai Trough subduction megathrust. *Science*, *356*(6343), 1157–1160. <https://doi.org/10.1126/science.aan3120>
- Avouac, J.-P. (2015). From geodetic imaging of seismic and aseismic fault slip to dynamic modeling of the seismic cycle. *Annual Review of Earth and Planetary Sciences*, *43*(1), 233–271. <https://doi.org/10.1146/annurev-earth-060614-105302>
- Axen, G. J. (1992). Pore pressure, stress increase, and fault weakening in low-angle normal faulting. *Journal of Geophysical Research*, *97*(B6), 8979–8991. <https://doi.org/10.1029/92JB00517>
- Axen, G. J. (2004). Mechanics of low-angle normal faults. In *Rheology and deformation of the lithosphere at continental margins* (pp. 46–91). New York City, NY: Columbia University Press. <https://doi.org/10.7312/karn12738-004>
- Axen, G. J. (2020). How a strong low-angle normal fault formed: The Whipple detachment, southeastern California. *GSA Bulletin*, *132*, 1817–1828. <https://doi.org/10.1130/b35386.1>
- Baldwin, S. L., Fitzgerald, P. G., & Webb, L. E. (2012). Tectonics of the New Guinea region. *Annual Review of Earth and Planetary Sciences*, *40*(1), 495–520. <https://doi.org/10.1146/annurev-earth-040809-152540>
- Banerjee, P., Pollitz, F. F., & Bürgmann, R. (2005). The size and duration of the Sumatra-Andaman earthquake from far-field static offsets. *Science*, *308*(5729), 1769–1772. <https://doi.org/10.1126/science.1113746>
- Beavan, J., Denys, P., Denham, M., Hager, B., Herring, T., & Molnar, P. (2010). Distribution of present-day vertical deformation across the Southern Alps, New Zealand, from 10 years of GPS data. *Geophysical Research Letters*, *37*, L16305. <https://doi.org/10.1029/2010GL044165>
- Beavan, J., Moore, M., Pearson, C., Henderson, M., Parsons, B., Bourne, S., et al. (1999). Crustal deformation during 1994–1998 due to oblique continental collision in the central Southern Alps, New Zealand, and implications for seismic potential of the Alpine fault. *Journal of Geophysical Research*, *104*(B11), 25,233–25,255. <https://doi.org/10.1029/1999jb900198>
- Beavan, J., Wallace, L. M., Palmer, N., Denys, P., Ellis, S., Fournier, N., et al. (2016). New Zealand GPS velocity field: 1995–2013. *New Zealand Journal of Geology and Geophysics*, *59*, 5–14. <https://doi.org/10.1080/00288306.2015.1112817>
- Behr, W. M., Kotowski, A. J., & Ashley, K. T. (2018). Dehydration-induced rheological heterogeneity and the deep tremor source in warm subduction zones. *Geology*, *46*(5), 475–478. <https://doi.org/10.1130/G40105.1>
- Bennett, R. A., Hreinsdóttir, S., Velasco, M. S., & Fay, N. P. (2007). GPS constraints on vertical crustal motion in the northern basin and range. *Geophysical Research Letters*, *34*, L22319. <https://doi.org/10.1029/2007GL031515>
- Biemiller, J., Wallace, L. M., Ellis, S. M., Little, T. A., Lavier, L., Mizera, M., & Webber, S. M. (2018). Short- and long-term deformation styles on an active low-angle normal fault: Mai'u fault, Papua New Guinea. *AGUFM*, 2018, T33D-T0430D.
- Bostock, M. G., Christensen, N. I., & Peacock, S. M. (2019). Seismicity in Cascadia. *Lithos*, *332–333*, 55–66. <https://doi.org/10.1016/j.lithos.2019.02.019>
- Boulton, C., Barth, N. C., Moore, D. E., Lockner, D. A., Townend, J., & Faulkner, D. R. (2018). Frictional properties and 3-D stress analysis of the southern Alpine Fault, New Zealand. *Journal of Structural Geology*, *114*, 43–54. <https://doi.org/10.1016/j.jsg.2018.06.003>
- Bürgmann, R. (2018). The geophysics, geology and mechanics of slow fault slip. *Earth and Planetary Science Letters*, *495*, 112–134. <https://doi.org/10.1016/j.epsl.2018.04.062>
- Burgmann, R., Schmidt, D., Nadeau, R. M., d'Alessio, M., Fielding, E., Manaker, D., et al. (2000). Earthquake potential along the Northern Hayward fault, California. *Science*, *289*(5482), 1178–1182. <https://doi.org/10.1126/science.289.5482.1178>
- Chen, J., Niemeijer, A. R., & Spiers, C. J. (2017). Microphysically derived expressions for rate-and-state friction parameters, a , b , and D_c . *Journal of Geophysical Research: Solid Earth*, *122*, 9627–9657. <https://doi.org/10.1002/2017JB014226>

- Chester, F. M., & Higgs, N. G. (1992). Multimechanism friction constitutive model for ultrafine quartz gouge at hypocentral conditions. *Journal of Geophysical Research*, 97(B2), 1859–1870. <https://doi.org/10.1029/91JB02349>
- Chiaraluce, L., Amato, A., Carannante, S., Castelli, V., Cattaneo, M., Cocco, M., et al. (2014). The alto Tiberina near fault observatory (northern Apennines, Italy). *Annals of Geophysics*, 57(3). <https://doi.org/10.4401/ag-6426>
- Chiaraluce, L., Chiarabba, C., Collettini, C., Piccinini, D., & Cocco, M. (2007). Architecture and mechanics of an active low-angle normal fault: Alto Tiberina Fault, northern Apennines, Italy. *Journal of Geophysical Research*, 112, B10310. <https://doi.org/10.1029/2007JB005015>
- Choi, E., & Buck, W. R. (2012). Constraints on the strength of faults from the geometry of rider blocks in continental and oceanic core complexes. *Journal of Geophysical Research*, 117, B04410. <https://doi.org/10.1029/2011JB008741>
- Choi, E., Buck, W. R., Lavier, L. L., & Petersen, K. D. (2013). Using core complex geometry to constrain fault strength. *Geophysical Research Letters*, 40, 3863–3867. <https://doi.org/10.1002/grl.50732>
- Collettini, C. (2011). The mechanical paradox of low-angle normal faults: Current understanding and open questions. *Tectonophysics*, 510(3–4), 253–268. <https://doi.org/10.1016/j.tecto.2011.07.015>
- Collettini, C., & Barchi, M. R. (2004). A comparison of structural data and seismic images for low-angle normal faults in the Northern Apennines (Central Italy): Constraints on activity. *Geological Society Special Publication*, 224(1), 95–112. <https://doi.org/10.1144/GSL.SP.2004.224.01.07>
- Collettini, C., Niemeijer, A., Viti, C., & Marone, C. (2009). Fault zone fabric and fault weakness. *Nature*, 462(7275), 907–910. <https://doi.org/10.1038/nature08585>
- Collettini, C., & Sibson, R. H. (2001). Normal faults, normal friction? *Geology*, 29(10), 927. [https://doi.org/10.1130/0091-7613\(2001\)029<0927:NFNF>2.0.CO;2](https://doi.org/10.1130/0091-7613(2001)029<0927:NFNF>2.0.CO;2)
- Collettini, C., Tesi, T., Scuderi, M. M., Carpenter, B. M., & Viti, C. (2019). Beyond Byerlee friction, weak faults and implications for slip behavior. *Earth and Planetary Science Letters*, 519, 245–263. <https://doi.org/10.1016/j.epsl.2019.05.011>
- Collettini, C., Viti, C., Smith, S. A. F., & Holdsworth, R. E. (2009). Development of interconnected talc networks and weakening of continental low-angle normal faults. *Geology*, 37(6), 567–570. <https://doi.org/10.1130/G25645A.1>
- Daczko, N. R., Caffi, P., Halpin, J. A., & Mann, P. (2009). Exhumation of the Dayman dome metamorphic core complex, eastern Papua New Guinea. *Journal of Metamorphic Geology*, 27(6), 405–422. <https://doi.org/10.1111/j.1525-1314.2009.00825.x>
- Dieterich, J. (1981). Constitutive properties of faults with simulated gouge. In N. L. Carter, M. Friedman, J. M. Logan, D. W. Stearns (Eds.), *Mechanical behavior of crustal rocks: The Handin Volume, Geophysical Monograph Series* (Vol. 24, pp. 103–120). American Geophysical Union. Retrieved from <https://agupubs.onlinelibrary.wiley.com/doi/abs/10.1029/GM024p0103>
- Dieterich, J. H. (1979). Modeling of rock friction: 1. Experimental results and constitutive equations. *Journal of Geophysical Research*, 84(B5), 2161. <https://doi.org/10.1029/JB084iB05p02161>
- Dziewonski, A. M., & Anderson, D. L. (1981). Preliminary reference Earth model *. *Physics of the Earth and Planetary Interiors*, 25.
- Ferris, A., Abers, G. A., Zelt, B., Taylor, B., & Roecker, S. (2006). Crustal structure across the transition from rifting to spreading: The Woodlark rift system of Papua New Guinea. *Geophysical Journal International*, 166(2), 622–634. <https://doi.org/10.1111/j.1365-246X.2006.02970.x>
- Floyd, J. S., Mutter, J. C., Goodliffe, A. M., & Taylor, B. (2001). Evidence for fault weakness and fluid flow within an active low-angle normal fault. *Nature*, 411(6839), 779–783. <https://doi.org/10.1038/35081040>
- Gu, J. C., Rice, J. R., Ruina, A. L., & Tse, S. T. (1984). Slip motion and stability of a single degree of freedom elastic system with rate and state dependent friction. *Journal of the Mechanics and Physics of Solids*, 32(3), 167–196. [https://doi.org/10.1016/0022-5096\(84\)90007-3](https://doi.org/10.1016/0022-5096(84)90007-3)
- Haines, S., Marone, C., & Saffer, D. (2014). Frictional properties of low-angle normal fault gouges and implications for low-angle normal fault slip. *Earth and Planetary Science Letters*, 408, 57–65. <https://doi.org/10.1016/j.epsl.2014.09.034>
- Harris, R. A. (2017). Large earthquakes and creeping faults. *Reviews of Geophysics*, 55, 169–198. <https://doi.org/10.1002/2016RG000539>
- Hayes, G. P. (2017). The finite, kinematic rupture properties of great-sized earthquakes since 1990. *Earth and Planetary Science Letters*, 468, 94–100. <https://doi.org/10.1016/j.epsl.2017.04.003>
- He, C., Luo, L., Hao, Q.-M., & Zhou, Y. (2013). Velocity-weakening behavior of plagioclase and pyroxene gouges and stabilizing effect of small amounts of quartz under hydrothermal conditions. *Journal of Geophysical Research: Solid Earth*, 118, 3408–3430. <https://doi.org/10.1002/jgrb.50280>
- Herring, T. A., Floyd, M. A., King, R. W., & McClusky, S. C. (2015). *GLOBK reference manual*. Cambridge, MA: Massachusetts Institute of Technology.
- Herring, T. A., King, R. W., Floyd, M. A., & McClusky, S. C. (2018). *GAMIT reference manual*. Cambridge, MA: Massachusetts Institute of Technology.
- Herring, T. A., Melbourne, T. I., Murray, M. H., Floyd, M. A., Szeliga, W. M., King, R. W., et al. (2016). Reviews of geophysics data analysis methods and geodetic products. *Reviews of Geophysics*, 54, 759–808. <https://doi.org/10.1002/2016RG000529>
- Hreinsdóttir, S., & Bennett, R. A. (2009). Active aseismic creep on the Alto Tiberina low-angle normal fault, Italy. *Geology*, 37(8), 683–686. <https://doi.org/10.1130/G30194A.1>
- Ikari, M. J., & Kopf, A. J. (2017). Seismic potential of weak, near-surface faults revealed at plate tectonic slip rates. *Science Advances*, 3(11), e1701269. <https://doi.org/10.1126/sciadv.1701269>
- Ikari, M. J., Marone, C., & Saffer, D. M. (2011). On the relation between fault strength and frictional stability. *Geology*, 39(1), 83–86. <https://doi.org/10.1130/G31416.1>
- Ikari, M. J., Saffer, D. M., & Marone, C. (2009). Frictional and hydrologic properties of clay-rich fault gouge. *Journal of Geophysical Research*, 114, B05409. <https://doi.org/10.1029/2008JB006689>
- Jackson, J., & McKenzie, D. (1983). The geometrical evolution of normal fault systems. *Journal of Structural Geology*, 5(5), 471–482. [https://doi.org/10.1016/0191-8141\(83\)90053-6](https://doi.org/10.1016/0191-8141(83)90053-6)
- Jackson, J. A. (1987). Active normal faulting and crustal extension. *Geological Society Special Publication*, 28(1), 3–17. <https://doi.org/10.1144/GSL.SP.1987.028.01.02>
- Jackson, J. A., & White, N. J. (1989). Normal faulting in the upper continental crust: Observations from regions of active extension. *Journal of Structural Geology*, 11(1–2), 15–36. [https://doi.org/10.1016/0191-8141\(89\)90033-3](https://doi.org/10.1016/0191-8141(89)90033-3)
- Koulali, A., Tregoning, P., McClusky, S., Stanaway, R., Wallace, L., & Lister, G. (2015). New insights into the present-day kinematics of the central and western Papua New Guinea from GPS. *Geophysical Journal International*, 202(2), 993–1004. <https://doi.org/10.1093/gji/ggv200>
- Lavier, L. L., Buck, W. R., & Poliakov, A. (1999). Self-consistent rolling-hinge model for the evolution of large-onset low-angle normal faults. *Geology*, 27(12), 1127–1130. [https://doi.org/10.1130/0091-7613\(1999\)027<1127:SCRHMF>2.3.CO;2](https://doi.org/10.1130/0091-7613(1999)027<1127:SCRHMF>2.3.CO;2)

- Lavier, L. L., Buck, W. R., & Poliakov, A. N. B. (2000). Factors controlling normal fault offset in an ideal brittle layer. *Journal of Geophysical Research*, 105(B10), 23,431–23,442. <https://doi.org/10.1029/2000JB900108>
- Lay, T., Kanamori, H., Ammon, C. J., Koper, K. D., Hutko, A. R., Ye, L., et al. (2012). Depth-varying rupture properties of subduction zone megathrust faults. *Journal of Geophysical Research*, 117, B04311. <https://doi.org/10.1029/2011JB009133>
- Lay, T., Ye, L., Ammon, C. J., & Kanamori, H. (2017). Intraslab rupture triggering megathrust rupture coseismically in the 17 December 2016 Solomon Islands M_w 7.9 earthquake. *Geophysical Research Letters*, 44, 1286–1292. <https://doi.org/10.1002/2017GL072539>
- Lee, S., Lin, T., Feng, K., & Liu, T. (2018). Composite megathrust rupture from deep interplate to trench of the 2016 Solomon Islands earthquake. *Geophysical Research Letters*, 45, 674–681. <https://doi.org/10.1002/2017GL076347>
- Leonard, M. (2010). Earthquake fault scaling: Self-consistent relating of rupture length, width, average displacement, and moment release. *Bulletin of the Seismological Society of America*, 100(5A), 1971–1988. <https://doi.org/10.1785/0120090189>
- Little, T. A., Baldwin, S. L., Fitzgerald, P. G., & Monteleone, B. (2007). Continental rifting and metamorphic core complex formation ahead of the Woodlark spreading ridge, D'Entrecasteaux Islands, Papua New Guinea. *Tectonics*, 26, TC1002. <https://doi.org/10.1029/2005TC001911>
- Little, T. A., Hacker, B. R., Gordon, S. M., Baldwin, S. L., Fitzgerald, P. G., Ellis, S., & Korchinski, M. (2011). Diapiric exhumation of Earth's youngest (UHP) eclogites in the gneiss domes of the D'Entrecasteaux Islands, Papua New Guinea. *Tectonophysics*, 510(1–2), 39–68. <https://doi.org/10.1016/j.tecto.2011.06.006>
- Little, T. A., Webber, S. M., Mizera, M., Boulton, C., Oesterle, J., Ellis, S., et al. (2019). Evolution of a rapidly slipping, active low-angle normal fault, Suckling-Dayman metamorphic core complex, SE Papua New Guinea. *GSA Bulletin*, 131(7–8), 1333–1363. <https://doi.org/10.1130/B35051.1>
- Lockner, D. A., Morrow, C., Moore, D., & Hickman, S. (2011). Low strength of deep San Andreas fault gouge from SAFOD core. *Nature*, 472(7341), 82–85. <https://doi.org/10.1038/nature09927>
- Malservisi, R., Furlong, K. P., & Gans, C. R. (2005). Microseismicity and creeping faults: Hints from modeling the Hayward fault, California (USA). *Earth and Planetary Science Letters*, 234(3–4), 421–435. <https://doi.org/10.1016/j.epsl.2005.02.039>
- Mann, P., Horton, B. K., Taylor, F. W., Shen, C., Lin, K., & Renema, W. (2009). Uplift patterns of reef terraces and sedimentary rocks constrain tectonic models for metamorphic core complexes in eastern Papua New Guinea. AGUFM, 2009, G33B-G0642B.
- Mann, P., & Taylor, F. W. (2002). Emergent Late Quaternary coral reefs of eastern Papua New Guinea constrain the regional pattern of oceanic ridge propagation. AGUFM, 2002, T52C-T1206C.
- Marone, C. (1998). Laboratory-derived friction laws and their application to seismic faulting. *Annual Review of Earth and Planetary Sciences*, 26(1), 643–696. <https://doi.org/10.1146/annurev.earth.26.1.643>
- Martinez, F., Goodliffe, A. M., & Taylor, B. (2001). Metamorphic core complex formation by density inversion and lower-crust extension. *Nature*, 411(6840), 930–934. <https://doi.org/10.1038/35082042>
- McCaffrey, R. (2009). Time-dependent inversion of three-component continuous GPS for steady and transient sources in northern Cascadia. *Geophysical Research Letters*, 36, L07304. <https://doi.org/10.1029/2008gl036784>
- Mizera, M., Little, T., Boulton, C., Biemiller, J., & Prior, D. (2020). Mixed-mode slip behavior and strength evolution of an actively exhuming low-angle normal fault, Woodlark Rift, SE Papua New Guinea, EGU General Assembly 2020, Online, 4–8 May 2020, EGU2020-EGU17399. <https://doi.org/10.5194/egusphere-egu2020-17399>
- Mizera, M., Little, T., Boulton, C., Prior, D. J., Watson, E. J., Biemiller, J. B., et al. (2020). Slow-to-fast deformation in mafic fault rocks on an active low-angle normal fault, Woodlark Rift, SE Papua New Guinea. *Geochemistry, Geophysics, Geosystems*, e2020GC009171. <https://doi.org/10.1029/2020GC009171>
- Mizera, M., Little, T. A., Biemiller, J., Ellis, S., Webber, S., & Norton, K. P. (2019). Structural and geomorphic evidence for rolling-hinge style deformation of an active continental low-angle normal fault, SE Papua New Guinea. *Tectonics*, 38, 1556–1583. <https://doi.org/10.1029/2018TC005167>
- Moore, D. E. (2014). Comparative mineral chemistry and textures of SAFOD fault gouge and damage-zone rocks. *Journal of Structural Geology*, 68(PA), 82–96. <https://doi.org/10.1016/j.jsg.2014.09.002>
- Moore, D. E., & Lockner, D. A. (2013). Chemical controls on fault behavior: Weakening of serpentinite sheared against quartz-bearing rocks and its significance for fault creep in the San Andreas system. *Journal of Geophysical Research: Solid Earth*, 118, 2558–2570. <https://doi.org/10.1002/jgrb.50140>
- Moore, D. E., Lockner, D. A., Ma, S., Summers, R., & Byerlee, J. D. (1997). Strengths of serpentinite gouges at elevated temperatures. *Journal of Geophysical Research*, 102(B7), 14,787–14,801. <https://doi.org/10.1029/97jb00995>
- Niemeijer, A. R., Boulton, C., Toy, V. G., Townend, J., & Sutherland, R. (2016). Large-displacement, hydrothermal frictional properties of DFDP-1 fault rocks, Alpine Fault, New Zealand: Implications for deep rupture propagation. *Journal of Geophysical Research: Solid Earth*, 121, 624–647. <https://doi.org/10.1002/2015JB012593>
- Niemeijer, A. R., & Collettini, C. (2014). Frictional properties of a low-angle normal fault under in situ conditions: Thermally-activated velocity weakening. *Pure and Applied Geophysics*, 171(10), 2641–2664. <https://doi.org/10.1007/s00024-013-0759-6>
- Niemeijer, A. R., Spiers, C. J., & Peach, C. J. (2008). Frictional behaviour of simulated quartz fault gouges under hydrothermal conditions: Results from ultra-high strain rotary shear experiments. *Tectonophysics*, 460, 288–303. <https://doi.org/10.1016/j.tecto.2008.09.003>
- Numelin, T., Kirby, E., Walker, J. D., & Didericksen, B. (2007). Late Pleistocene slip on a low-angle normal fault, Searles Valley, California. *Geosphere*, 3(3), 163–176. <https://doi.org/10.1130/GES00052.1>
- Numelin, T., Marone, C., & Kirby, E. (2007). Frictional properties of natural fault gouge from a low-angle normal fault, Panamint Valley, California. *Tectonics*, 26, TC2004. <https://doi.org/10.1029/2005TC001916>
- Okada, Y. (1985). Surface deformation due to shear and tensile faults in a half-space. *Bulletin of the Seismological Society of America*, 75(4), 1135–1154.
- Okamoto, A. S., Niemeijer, A. R., Takeshita, T., Verberne, B. A., & Spiers, C. J. (2020). Frictional properties of actinolite-chlorite gouge at hydrothermal conditions. *Tectonophysics*, 779, 228377. <https://doi.org/10.1016/j.tecto.2020.228377>
- Okamoto, A. S., Verberne, B. A., Niemeijer, A. R., Takahashi, M., Shimizu, I., Ueda, T., & Spiers, C. J. (2019). Frictional properties of simulated chlorite gouge at hydrothermal conditions: Implications for subduction megathrusts. *Journal of Geophysical Research: Solid Earth*, 124, 4545–4565. <https://doi.org/10.1029/2018JB017205>
- Osterle, J. E., Little, T. A., Seward, D., Stockli, D. F., & Gamble, J. (2020). The petrology, geochronology and tectono-magmatic setting of igneous rocks in the Suckling-Dayman metamorphic core complex, Papua New Guinea. *Gondwana Research*, 83, 390–414. <https://doi.org/10.1016/j.jgr.2020.01.014>
- Platt, J. P., Behr, W. M., & Cooper, F. J. (2015). Metamorphic core complexes: Windows into the mechanics and rheology of the crust. *Journal of the Geological Society*, 172(1), 9–27. <https://doi.org/10.1144/jgs2014-036>

- Pollitz, F. F. (1996). Coseismic deformation from earthquake faulting on a layered spherical Earth. *Geophysical Journal International*, 125(1), 1–14. <https://doi.org/10.1111/j.1365-246X.1996.tb06530.x>
- Reinen, L. A., & Weeks, J. D. (1993). Determination of rock friction constitutive parameters using an iterative least squares inversion method. *Journal of Geophysical Research*, 98(B9), 15,937–15,950. <https://doi.org/10.1029/93JB00780>
- Rice, J. R., & Tse, S. T. (1986). Dynamic motion of a single degree of freedom system following a rate and state dependent friction law. *Journal of Geophysical Research*, 91(B1), 521. <https://doi.org/10.1029/JB091iB01p00521>
- Ruina, A. (1983). Slip instability and state variable friction laws. *Journal of Geophysical Research*, 88(B12), 10,359–10,370. <https://doi.org/10.1029/JB088iB12p10359>
- Ruppel, C. (1995). Extensional processes in continental lithosphere. *Journal of Geophysical Research*, 100(B12), 24,187–24,215. <https://doi.org/10.1029/95jb02955>
- Scholz, C. H. (2019). *The mechanics of earthquakes and faulting* (3rd ed.). Cambridge: Cambridge University Press. <https://doi.org/10.1017/9781316681473>
- Schwartz, S., Guillot, S., Reynard, B., Lafay, R., Debret, B., Nicollet, C., et al. (2013). Pressure-temperature estimates of the lizardite/antigorite transition in high pressure serpentinites. *Lithos*, 178, 197–210. <https://doi.org/10.1016/j.lithos.2012.11.023>
- Schwartz, S. Y., & Rokosky, J. M. (2007). Slow slip events and seismic tremor at circum-Pacific subduction zones. *Reviews of Geophysics*, 45, RG3004. <https://doi.org/10.1029/2006RG000208>
- Segall, P. (2010). *Earthquake and volcano deformation*. Princeton, NJ: Princeton University Press.
- Serpelloni, E., Faccenna, C., Spada, G., Dong, D., & Williams, S. D. P. (2013). Vertical GPS ground motion rates in the Euro-Mediterranean region: New evidence of velocity gradients at different spatial scales along the Nubia-Eurasia plate boundary. *Journal of Geophysical Research: Solid Earth*, 118, 6003–6024. <https://doi.org/10.1002/2013JB010102>
- Smith, S. A. F., & Faulkner, D. R. (2010). Laboratory measurements of the frictional properties of the Zuccale low-angle normal fault, Elba Island, Italy. *Journal of Geophysical Research*, 115, B02407. <https://doi.org/10.1029/2008JB006274>
- Sone, H., Shimamoto, T., & Moore, D. E. (2012). Frictional properties of saponite-rich gouge from a serpentinite-bearing fault zone along the Gokasho-Arashima Tectonic Line, central Japan. *Journal of Structural Geology*, 38, 172–182. <https://doi.org/10.1016/j.jsg.2011.09.007>
- Strasser, F. O., Arango, M. C., & Bommer, J. J. (2010). Scaling of the source dimensions of interface and intraslab subduction-zone earthquakes with moment magnitude. *Seismological Research Letters*, 81(6), 941–950. <https://doi.org/10.1785/gssrl.81.6.941>
- Taylor, B., Goodliffe, A. M., & Martinez, F. (1999). How continents break up: Insights from Papua New Guinea. *Journal of Geophysical Research*, 104(B4), 7497–7512. <https://doi.org/10.1029/1998jb900115>
- Taylor, F. W., Briggs, R. W., Frohlich, C., Brown, A., Hornbach, M., Papabatu, A. K., et al. (2008). Rupture across arc segment and plate boundaries in the 1 April 2007 Solomons earthquake. *Nature Geoscience*, 1(4), 253–257. <https://doi.org/10.1038/ngeo159>
- Tjhin, K. T. (1976). Trobriand Basin exploration, Papua New Guinea. *The APPEA Journal*, 16(1), 81. <https://doi.org/10.1071/aj75008>
- Tregoning, P., Burgette, R., McClusky, S. C., Lejeune, S., Watson, C. S., & McQueen, H. (2013). A decade of horizontal deformation from great earthquakes. *Journal of Geophysical Research: Solid Earth*, 118, 2371–2381. <https://doi.org/10.1002/jgrb.50154>
- U.S. Geological Survey. (2019). Earthquake hazards program.
- Valoroso, L., Chiaraluze, L., Di Stefano, R., & Monachesi, G. (2017). Mixed-mode slip behavior of the Altotiberina low-angle Normal fault system (northern Apennines, Italy) through high-resolution earthquake locations and repeating events. *Journal of Geophysical Research: Solid Earth*, 122, 10,220–10,240. <https://doi.org/10.1002/2017JB014607>
- Wallace, L. M., Ellis, S., Little, T., Tregoning, P., Palmer, N., Rosa, R., et al. (2014). Continental breakup and UHP rock exhumation in action: GPS results from the Woodlark Rift, Papua New Guinea. *Geochemistry, Geophysics, Geosystems*, 15, 4267–4290. <https://doi.org/10.1002/2014GC005458>
- Wallace, L. M., Taylor, F. W., Bevis, M. G., Phillips, D. A., Walter, J. I., Kendrick, E. C., & Papabatu, A. K. (2015). Interseismic, coseismic, postseismic, and slow slip event deformation above a shallow subduction thrust in the western Solomon Islands. *AGU Fall Meeting Abstracts*, 2015, T44B-T07B.
- Webber, S., Little, T. A., Norton, K. P., Österle, J., Mizera, M., Seward, D., & Holden, G. (2020). Progressive back-warping of a rider block atop an actively exhuming, continental low-angle normal fault. *Journal of Structural Geology*, 130, 103906. <https://doi.org/10.1016/j.jsg.2019.103906>
- Webber, S., Norton, K. P., Little, T. A., Wallace, L. M., & Ellis, S. (2018). How fast can low-angle normal faults slip? Insights from cosmogenic exposure dating of the active Mai'iu fault, Papua New Guinea. *Geology*, 46(3), 227–230. <https://doi.org/10.1130/G39736.1>
- Wernicke, B. (1995). Low-angle normal faults and seismicity: A review. *Journal of Geophysical Research*, 100(B10), 20,159–20,174. <https://doi.org/10.1029/95JB01911>
- Williams, S. D. P., Bock, Y., Fang, P., Jamason, P., Nikoladi, R., Prawirodirdjo, L., et al. (2004). Error analysis of continuous GPS position time series. *Journal of Geophysical Research*, 109, B03412. <https://doi.org/10.1029/2003JB002741>
- Wolfson-Schwehr, M., & Boettcher, M. S. (2019). Global characteristics of oceanic transform fault structure and seismicity. In *Transform plate boundaries and fracture zones* (pp. 21–59). Cambridge, MA: Elsevier. <https://doi.org/10.1016/b978-0-12-812064-4.00002-5>
- Yuan, X. P., Olive, J.-A., & Braun, J. (2020). Partially locked low-angle normal faults in cohesive Upper Crust. *Tectonics*, 39, e2019TC005753. <https://doi.org/10.1029/2019tc005753>
- Zhang, J., Bock, Y., Johnson, H., Fang, P., Williams, S., Genrich, J., et al. (1997). Southern California permanent GPS geodetic array: Error analysis of daily position estimates and site velocities. *Journal of Geophysical Research*, 102(B8), 18,035–18,055. <https://doi.org/10.1029/97jb01380>